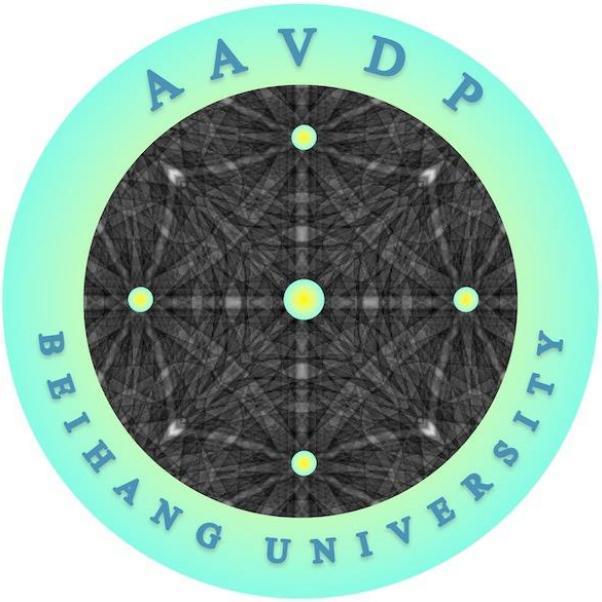

User Manual

Version 1.0.0, Jan 04, 2025

Edit by

Yan Zhang

Ruifeng Zhang

M I C I D

Materials Integrated Computation and Intelligent Design

Contents

1 Introduction

AAVDP (Automatic Analysis of Virtual Diffraction Pattern) is a program developed by the MICID team at Beihang University for diffraction simulations and analyses. It aims to address the diffraction challenges associated with fields such as crystallography, physics, chemistry, and materials science, and facilitate the scientific researches of crystal structures and defects. Although existing programs offer some diffraction functionalities, they are often limited in terms of their extensibility, automation, and visualization. For example, LAMMPS [1], a program widely used for molecular dynamics (MD), supports X-ray and electron diffraction but lacks the ability for Kikuchi diffraction and the feature of in situ visualization. Some third-party packages, such as EMSOFT [2], provide available diffraction and visualization tools, but require cumbersome installation and operation, which limits accessibility for new users. AAVDP overcomes these limitations by offering a light-weight, easy-to-use interface and powerful diffraction functions, allowing researchers to efficiently and accurately simulate and analyze diffraction patterns.

AAVDP is developed using C/C++ programming languages, with a small volume and features of high efficiency and stability. The program supports running on Windows, Linux, or macOS systems, ensuring strong portability and cross-platform capability. The software streamlines the entire process, including structure extraction, diffraction simulations, pattern analyses, and in situ imaging. Furthermore, AAVDP can be easily integrated into the SPaMD platform [3], providing users with automated diffraction workflows.

In summary, AAVDP is a powerful and user-friendly tool for diffraction simulations and analyses, offering valuable support for researchers in the fields of crystallography, materials science, physics, and chemistry.

2 Configuration and installation

Requiring AAVDP:

1. Download directly from the MICID website at http://micid.top/softwares/aavdp
2. Download directly from the GitHub repository at https://github.com/zrfcms/aavdp
3. Send a registration form to zrfcms@buaa.edu.cn and require a download link for Baidu Cloud Drive

Running AAVDP:

On Windows system

>>tar -xvf AAVDP-x.x.x.tar.gz (or unzip AAVDP-x.x.x.zip)

>>cd AAVDP-x.x.x

>>./bin/AAVDP_win.exe -h

If the terminal displays the following information, the program is running correctly:

```
PS C:                    \aavdp> .\bin\AAVDP_win.exe -h
The syntax format and rules for AAVDP:
    AAVDP <--mode> (inputfile) <-parameter> [value]
    AAVDP --xrd     # X-ray diffraction
    AAVDP --ned     # Neutron diffraction
    AAVDP --ked     # Kinematic electron diffraction
    AAVDP --ded     # Dynamical electron diffraction
    AAVDP --kkd     # Kinematic Kikuchi diffraction
    AAVDP --dkd     # Dynamical Kikuchi diffraction
    AAVDP --rdf     # Radial distribution function
    AAVDP --ssf     # Static structure factor
Try 'AAVDP -h [mode]' for more information, e.g., 'AAVDP -h xrd'
```

Note: To guarantee the smooth operation of AAVDP_win.exe, make sure that five specific .dll files are in the same directory as AAVDP_win.exe, including cyggcc_s-

seh-1.dll, cyggfortran-5.dll, cygquadmath-0.dll, cygstdc++-6.dll, cygwin1.dll.

On Linux system

>>tar -xvf AAVDP-x.x.x.tar.gz (or unzip AAVDP-x.x.x.zip)

>>cd AAVDP-x.x.x

>>./bin/AAVDP_linux -h

If the terminal displays the following information, the program is running correctly:

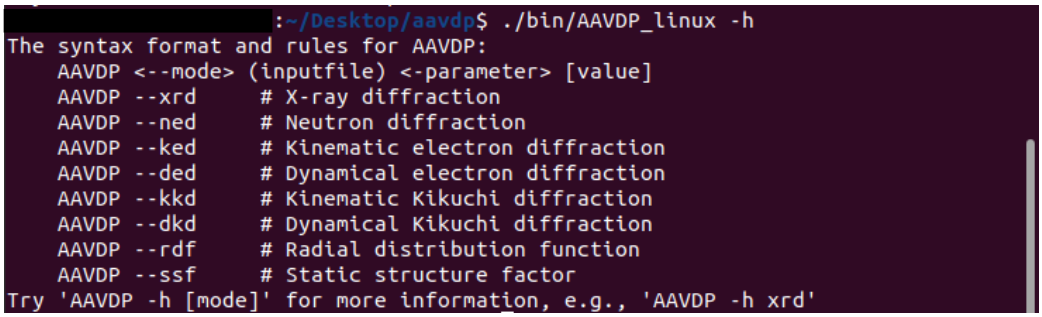

On macOS system

>>tar -xvf AAVDP-x.x.x.tar.gz (or unzip AAVDP-x.x.x.zip)

>>cd AAVDP-x.x.x

>>./bin/AAVDP_mac -h

If the terminal displays the following information, the program is running correctly:

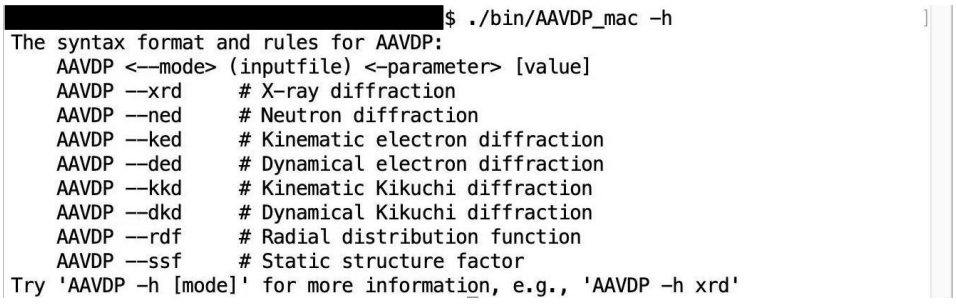

Note: The above executable files were compiled on the Windows 11, Ubuntu 22.04, macOS Big Sur 11.7.4 platforms, respectively. The compilation steps are provided below.

Compiling AAVDP:

On Windows system

(1) Download setup-x86_64.exe from the Cygwin website and double-click it to start the installation. The key steps are as follows:

a. Choose A Download Source: It is recommended to select “Install from Internet (downloaded files will be kept for future re-use)”.

b. Select Root Install Directory: It is user-defined.

c. Select Local Package Directory: It is user-defined.

d. Select Your Internet Connection: It is recommended to select “Use System Proxy Settings”.

e. Choose A Download Site: It is user-defined.

f. Select Packages: It is necessary to select and install related compiler installation packages with specified versions, including binutils (v2.43.1-1), gcc-gfortran (v12.4.0-3), gcc-g++ (v12.4.0-3), gdb (v13.2-1), and make (v4.4.1-2).

Start the Cygwin64 terminal after the installation.

Note: It is recommended to keep the setup-x86_64.exe, since it can be re-used for installing or uninstalling package components if necessary.

(2) Compile dependency libraries and store compiled files in specific directories, i.e., .a files in /lib/win and .h files in /include (both directories are pre-populated with compiled files for the Windows 11 platform):

a. Download lapack-3.12.0.tar.gz from the LAPACK — Linear Algebra PACKage

(netlib.org) website. In the Cygwin64 terminal, execute the following commands:

```
>>tar -xvf lapack-3.12.0.tar.gz
>>cd lapack-3.12.0
>>cp make.inc.example make.inc
>>make blaslib
>>make cblaslib
>>make lapacklib
>>make lapackelib
```

After running the above commands, the following static library files will be generated in the lapack-3.12.0 directory: librefblas.a, libcblas.a, liblapack.a, and liblapacke.a. Header files will be generated in the lapack-3.12.0/CBLAS/include and lapack-3.12.0/LAPACKE/include directories: lapack.h, lapacke.h, and lapacke_mangling.h.

Note: The LAPACK library depends on the Fortran library. Copy the libgfortran.dll.a file from the Cygwin installation directory to /lib/win.

b. Download zlib-1.3.1.tar.gz from the zlib Home Site website and libpng-1.6.43.tar.gz from the LIBPNG: PNG reference library - Browse /libpng16/1.6.43 at SourceForge.net website. In the Cygwin64 terminal, execute the following commands:

For zlib:

```
>>tar -xvf  zlib-1.3.1.tar.gz
>>cd zlib-1.3.1
>>./configure --prefix=[libpng_src_directory]
>>make && make install
```

For libpng:

>>tar -xvf libpng-1.6.43.tar.gz

>>cd libpng-1.6.43

>>./configure --prefix=[libpng_src_directory] LIBS=-L[libpng_src_directory]/lib CPPFLAGS=-I[libpng_src_directory]/include

>> make && make install

In the [libpng_src_directory]/lib directory, the following static library files will be generated: libz.a, libpng16.a, and libpng16.la. Header files will be generated in the [libpng_src_directory]/include and [libpng_src_directory]/include/libpng16 directories: png.h, pngconf.h, pnglibconf.h, zconf.h, and zlib.h.

Note: The user-defined [libpng_src_directory] must be an absolute path.

(3) Download AAVDP-x.x.x.tar.gz or AAVDP-x.x.x.zip. In the Cygwin64 terminal, execute the following commands:

>>tar -xvf AAVDP-x.x.x.tar.gz (or unzip AAVDP-x.x.x.zip)

>>cd AAVDP-x.x.x

>>cp makefile.win makefile

>>make

AAVDP_win.exe will be generated in /bin.

On Linux system

(1) Install the GNU compilers: Start the terminal and execute the following commands:

>>sudo apt install gcc (and g++ and gfortran and make)

>>gcc (and g++ and gfortran and make) -v

(2) Compile dependency libraries and store compiled files in specific directories, i.e., .a files in /lib/linux and .h files in /include (both directories are pre-populated with compiled files for the Ubuntu 22.04 platform):

a. Download lapack-3.12.0.tar.gz from the LAPACK — Linear Algebra PACKage (netlib.org) website. In the Cygwin64 terminal, execute the following commands:

>>tar -xvf lapack-3.12.0.tar.gz

>>cd lapack-3.12.0

>>cp make.inc.example make.inc

>>make blaslib

>>make cblaslib

>>make lapacklib

>>make lapackelib

After running the above commands, the following static library files will be generated in the lapack-3.12.0 directory: librefblas.a, libcblas.a, liblapack.a, and liblapacke.a. Header files will be generated in the lapack-3.12.0/CBLAS/include and lapack-3.12.0/LAPACKE/include directories: lapack.h, lapacke.h, and lapacke_mangling.h.

Note: The LAPACK library depends on the Fortran library. Copy the libgfortran.a and libquadmath.a files from the system directory to /lib/linux.

b. Download zlib-1.3.1.tar.gz from the zlib Home Site website and libpng-1.6.43.tar.gz from the LIBPNG: PNG reference library - Browse /libpng16/1.6.43 at SourceForge.net website. In the terminal, execute the following commands:

For zlib:

>>tar -xvf zlib-1.3.1.tar.gz

>>cd zlib-1.3.1

>>./configure --prefix=[libpng_src_directory]

>>make && make install

For libpng:

>>tar -xvf libpng-1.6.43.tar.gz

>>cd libpng-1.6.43

>>./configure --prefix=[libpng_src_directory] LIBS=-L[libpng_src_directory]/lib CPPFLAGS=-I[libpng_src_directory]/include

>> make && make install

In the [libpng_src_directory]/lib directory, the following static library files will be generated: libz.a, libpng16.a, and libpng16.la. Header files will be generated in the [libpng_src_directory]/include and [libpng_src_directory]/include/libpng16 directories: png.h, pngconf.h, pnglibconf.h, zconf.h, and zlib.h.

Note: The user-defined [libpng_src_directory] must be an absolute path and under the system directory /usr/local for ensuring that the installation of libpng-1.6.43 can correctly identify whether zlib-1.3.1 is installed.

(3) Download AAVDP-x.x.x.tar.gz or AAVDP-x.x.x.zip. In the terminal, execute the following commands:

>>tar -xvf AAVDP-x.x.x.tar.gz (or unzip AAVDP-x.x.x.zip)

>>cd AAVDP-x.x.x

>>cp makefile.linux makefile

>>make

AAVDP_linux will be generated in /bin.

On macOS system

(1) Install compilers: By default, macOS has Clang versions of gcc, g++, and GNU version of make pre-installed, which can be verified by checking the version:

>>gcc (and g++ and make) -v

The gfortran compiler is not pre-installed, of which installer can be downloaded from the Releases · fxcoudert/gfortran-for-macOS · GitHub website and double-clicked to start the installation. For example, if macOS Big Sur 11.7.4 is used, download the gfortran-Intel-11.2-BigSur.dmg. The gfortran will be installed in /usr/local/gfortran by default.

(2) Compile dependency libraries and store compiled files in specific directories, i.e., .a files in /lib/mac and .h files in /include (both directories are pre-populated with compiled files for the macOS Big Sur 11.7.4 platform):

a. Download lapack-3.12.0.tar.gz from the LAPACK — Linear Algebra PACKage (netlib.org) website. In the terminal, execute the following commands:

>>tar -xvf lapack-3.12.0.tar.gz

>>cd lapack-3.12.0

>>cp make.inc.example make.inc

>>make blaslib

>>make cblaslib

>>make lapacklib

>>make lapackelib

After running the above commands, the following static library files will be generated in the lapack-3.12.0 directory: librefblas.a, libcblas.a, liblapack.a, and liblapacke.a. Header files will be generated in the lapack-3.12.0/CBLAS/include and lapack-3.12.0/LAPACKE/include directories: lapack.h, lapacke.h, and lapacke_mangling.h.

Note: The LAPACK library depends on the Fortran library. Copy the libgfortran.a and libquadmath.a files from the /usr/local/gfortran/lib directory to /lib/mac, along with libgcc.a file from the /usr/local/gfortran/lib/gcc/x86_64-apple-darwin20/11.2.0 directory.

b. Download zlib-1.3.1.tar.gz from the zlib Home Site website and libpng-1.6.43.tar.gz from the LIBPNG: PNG reference library - Browse /libpng16/1.6.43 at SourceForge.net website. In the terminal, execute the following commands:

For zlib:

>>tar -xvf zlib-1.3.1.tar.gz

>>cd zlib-1.3.1

>>./configure --prefix=[libpng_src_directory]

>>make && make install

For libpng:

>>tar -xvf libpng-1.6.43.tar.gz

>>cd libpng-1.6.43

>>./configure --prefix=[libpng_src_directory] LIBS=-L[libpng_src_directory]/lib

CPPFLAGS=-I[libpng_src_directory]/include

>> make && make install

In the [libpng_src_directory]/lib directory, the following static library files will be generated: libz.a, libpng16.a, and libpng16.la. Header files will be generated in the [libpng_src_directory]/include and [libpng_src_directory]/include/libpng16 directories: png.h, pngconf.h, pnglibconf.h, zconf.h, and zlib.h.

Note: The user-defined [libpng_src_directory] must be an absolute path.

(3) Download AAVDP-x.x.x.tar.gz or AAVDP-x.x.x.zip. In the terminal, execute the following commands:

>>tar -xvf AAVDP-x.x.x.tar.gz (or unzip AAVDP-x.x.x.zip)

>>cd AAVDP-x.x.x

>>cp makefile.mac makefile

>>make

AAVDP_mac will be generated in /bin.

3 Background

Diffraction is a phenomenon in which a wave deviate from its original direction of propagation when encountering an obstacle or a slit. Due to the interaction between incident waves and crystalline materials with atomic periodic arrangement, the interference between diffracted waves produces diffraction patterns and Kikuchi patterns. These patterns serve as crucial crystallographic fingerprints that reveal characteristics of structures, phases, orientations, and etc. Based on the source of

incident wave, diffraction techniques can be classified into X-ray diffraction, neutron diffraction, and electron diffraction.

Virtual Diffraction Pattern (VDP) technology is used for simulating diffraction and analyzing patterns from crystalline or amorphous models, which plays a crucial role in both scientific researches and technological applications. VDP not only facilitates studying crystal or amorphous structures but also helps exploring the properties, performances, and applications of materials. With its broad applicability in fields like crystallography and materials science, it is confirmed that VDP provides significant technological support to researchers.

3.1 Basic theory

3.1.1 Crystal lattice and Bragg's equation

In an ideal crystal, atoms, ions, or etc. are abstracted as geometric points arranged regularly in three-dimensional space and having identical environments. These points are named as lattice points and the regular arrangement is called the lattice. If three basic vectors of the crystal lattice are represented by $\mathbf{a}$, $\mathbf{b}$, and $\mathbf{c}$, the lattice point $\mathbf{r}$ is given below:

$$\mathbf{r} = u\mathbf{a} + v\mathbf{b} + w\mathbf{c} \tag{3.1.1}$$

The reduced $[uvw]$ represents a crystallographic direction, and (hkl)indicates the crystallographic plane perpendicular to $[uvw]$ $(hu + kv + wl = 0)$.

Researches of crystal structures primarily depends on analyzing diffraction phenomena between the incident wave and the target crystal. The foundation of

diffraction analysis is Bragg's equation:

$$2d_{HKL}\sin\theta = \lambda \tag{3.1.2}$$

where (HKL) are diffraction indices and related to (hkl) by $H = nh$, $K = nk$, and $L = nl$ (n is an integer); and d_{HKL} is the interplanar spacing between the (HKL) planes; θ is the half of diffraction angle, i.e., the angle between the incident and diffracted waves; λ is the wavelength of the incident wave. The virtual (HKL) planes are extended from the real (hkl) planes. The first-order diffraction on (HKL) planes corresponds to the n-order diffraction on (hkl) planes. As the Bragg's equation is satisfied, constructive interference occurs between the diffracted waves from adjacent (HKL) planes; Conversely, interference is weakened.

3.1.2 Reciprocal lattice and diffraction vector equation

The reciprocal lattice is established based on the crystal lattice through certain mathematical transformation. If three basis vectors in the reciprocal lattice are denoted by $\mathbf{a}^*$, $\mathbf{b}^*$, and $\mathbf{c}^*$. The relationships between the crystal lattice and reciprocal lattice are as follows:

$$\begin{aligned}\mathbf{a}^* &= \frac{\mathbf{b}\times\mathbf{c}}{\mathbf{a}\cdot(\mathbf{b}\times\mathbf{c})}\\ \mathbf{b}^* &= \frac{\mathbf{c}\times\mathbf{a}}{\mathbf{a}\cdot(\mathbf{b}\times\mathbf{c})}\\ \mathbf{c}^* &= \frac{\mathbf{a}\times\mathbf{b}}{\mathbf{a}\cdot(\mathbf{b}\times\mathbf{c})}\end{aligned} \tag{3.1.3}$$

The reciprocal point $\mathbf{g}$ can be expressed as:

$$\mathbf{g} = h\mathbf{a}^* + k\mathbf{b}^* + l\mathbf{c}^* \tag{3.1.4}$$

Two important conclusions can be deduced: The reciprocal vector $\mathbf{g}_{hkl}$ is

perpendicular to the (hkl) planes; The magnitude of the reciprocal vector g_{hkl} is the inverse of the interplanar spacing d_{hkl} between the (hkl) planes.

If the incident and diffracted waves are respectively represented by the unit vectors $\mathbf{s}_0$ and $\mathbf{s}_1$, the Bragg's equation can be formulated as the diffraction vector equation:

$$\frac{\mathbf{s}_1}{\lambda} - \frac{\mathbf{s}_0}{\lambda} = \mathbf{g}_{HKL} \tag{3.1.5}$$

Furthermore, if the incident and diffracted waves are respectively represented by the wave vectors $\mathbf{k}_0$ and $\mathbf{k}_1$, the diffraction equation can be rewritten as:

$$\mathbf{k} = \mathbf{k}_1 - \mathbf{k}_0 = \mathbf{g}_{HKL} \tag{3.1.6}$$

Assuming that $\mathbf{k}_0$ starts from the C (the center of the Ewald sphere with a radius of k_0), and ends as the O* (the origin of reciprocal space), it can be deduced from the equation (3.1.6) that $\mathbf{g}$ located on the surface of Ewald sphere satisfies the condition of constructive interference. This is known as the Ewald diagram.

3.2 X-ray and neutron diffraction

Since X-ray diffraction was discovered by Max von Laue in 1912, the technique has evolved from Laue's method and the Debye-Scherrer method to the powder diffractometer method. Currently, X-ray diffraction is one of the most widely used tools for testing and analysis in materials.

X-rays are electromagnetic waves with wavelengths ranging from 0.1 to 10 Å, traveling at the speed of light. They are generated as high-energy electron beams strike a metal target, e.g., $\mathrm{Cu-K}_\alpha$ radiation ($\lambda = 1.54184$Å). As X-rays illuminate

the sample, coherent scattering occurs on electrons that are tightly bound to atomic nuclei. In this case, all scattered waves retain the same wavelength as the incident waves and form a phase relationship; incoherent scattering occurs when X-rays interact with free or loosely bound electrons, resulting in scattered waves with different wavelengths. The coherent scattering causes constructive interference and lays the theoretical basis of X-ray diffraction along with Bragg's law. X-ray diffraction has characteristics of non-destructive analysis, strong penetration, and resistance to electromagnetic fields. It is widely employed for precise determination of lattice constant, residual stress, crystallinity, and so on.

The diffraction intensity $I_x(\mathbf{g})$ is calculated as below [4]:

$$I_x(\mathbf{g}) = L_p(\theta) \cdot \frac{F(\mathbf{g}) \cdot F(\mathbf{g})^*}{N} \qquad (3.2.1)$$
$$\frac{\sin\theta}{\lambda} = \frac{|\mathbf{g}|}{2}$$

Here, $F(\mathbf{g})$ is the structure factor, N is the total number of atoms, and $F(\mathbf{g})$is expressed as:

$$F(\mathbf{g}) = \sum_{j=1}^{N} f_j(\theta) \cdot \exp\left(2\pi i \mathbf{g} \cdot \mathbf{r}_j\right) \qquad (3.2.2)$$

where $f_j(\theta)$ is the atomic scattering factor for the j-th atom; and $\mathbf{r}_j$ is the spatial position of the j-th atom. The $f_j(\theta)$ is given by:

$$f_j(\theta) = e^{-M_j(\theta)} f_j^0(\theta) \qquad (3.2.3)$$

$f_j^0(\theta)$ is the atomic scattering factor at temperature of 0 K, and can be approximated as the following Gaussian formula [5]:

$$f_j^0\left(\frac{\sin\theta}{\lambda}\right) = \sum_{i}^{4} a_i \exp\left(-b_i \frac{\sin^2\theta}{\lambda^2}\right) + c \qquad (3.2.4)$$

with coefficients a_i, b_i, and c available from the Atomic form factors (tugraz.at) website. The temperature factor $e^{-M_j(\theta)}$ is given by:

$$M_j\left(\frac{\sin\theta}{\lambda}\right) = B_j(T)\frac{\sin^2\theta}{\lambda^2} \tag{3.2.5}$$

with Debye-Waller factor $B_j(T)$ [6].

The reciprocal points $\mathbf{g}$ are obtained based on the sampling scheme proposed by Coleman et al. [4], which is applicable to both crystalline and defective models, as shown in Fig. 1. A three-dimensional orthogonal or oblique reciprocal mesh is constructed using reciprocal axes $\mathbf{x}_1^*$, $\mathbf{x}_2^*$, and $\mathbf{x}_3^*$of the simulation cell, with their spacings c_1^*, c_2^*, and c_3^*as the inverse of simulation dimensions or user-defined values. In this mesh, a reciprocal sphere with radius of $2k_0$is obtained by rotating the Ewald sphere around the O* and defines reciprocal points $\mathbf{g}$ to be considered. This design is consistent with the operational condition of a powder diffractometer, where all crystal orientations (or incident directions) is equally accessed.

$I_x(\theta)$ requires additional multiplicity factor P_{hkl} and the Lorentz-polarization factor L_p compared with $I_x(\mathbf{g})$. The multiplicity factor refers to the number of $\{hkl\}$ planes, which corresponds to the number of equivalent reciprocal vectors $\mathbf{g}$. The Lorentz factor [7] is related to the diffraction geometry and given by $1/\sin 2\theta$ for a small crystal, $1/(\cos(\theta)\sin^2(\theta))$ for a powder polycrystal, while the polarization factor quantifies the polarization during the coherent scattering between a non-polarized X-ray and a single electron and is calculated as $(1+\cos^2(2\theta))/2$.

Using the above formulas, $I-2\theta$ profile can be generated, with I in arbitrary units (a.u.). The profile for single crystals exhibits diffraction lines at specific 2θ,

while the curve for polycrystals with random grain orientations displays diffraction peaks. The peaks can be described using the pseudo-Voigt function proposed by Giacovazzo et al. [7]:

$$I_x(\theta) = I_x(\theta_k)\left[\eta\frac{\sqrt{C_0}}{\pi\omega_k}\frac{1}{1+C_0X_k^2} + (1-\eta)\frac{\sqrt{C_1}}{\sqrt{\pi}\omega_k}\mathrm{e}^{-C_1X_k^2}\right] \tag{3.2.6}$$

where $C_0 = 4$ and $C_1 = 4\ln 2$; η is the mixing parameter, with $\eta = 1$ corresponding to the pure Lorentzian and $\eta = 0$ to the pure Gaussian; $X_k \equiv 2(\theta - \theta_k)/\omega_k$, and $\omega_k$is the full width at half maximum (FWHM) of the diffraction peak k, which can be obtained from the Scherrer formula:

$$\omega_k(RAD) = \frac{0.90\lambda}{D\cos\theta_k} \tag{3.2.7}$$

Neutron diffraction is another technique widely used for testing and analysis. Neutrons are electrically neutral, slightly heavier than photons, and possess strong penetration. Their de Broglie wavelength is approximately 1.0 Å, which is comparable to atomic spacing. Neutrons mainly interact with atomic nuclei, inducing both elastic and inelastic scattering. After the elastic scattering, neutrons alter their directions without losing energy, while the inelastic scattering involves energy loss. Additionally, since the scattering sources are the atomic nuclei rather than the electron cloud, $I_n(\theta)$ differs from $I_x(\theta)$ in two ways: the polarization factor is not required; $f_j^0(\theta)$ is constant and represented by the atomic scattering length b_j^c, which is highly sensitive to atomic mass. Therefore, neutron diffraction is especially useful for identifying isotopes and studying chemical ordering in transition metals or alloys. For more information, the b_j^c is available on the Neutron scattering lengths and cross sections (nist.gov) website [8].

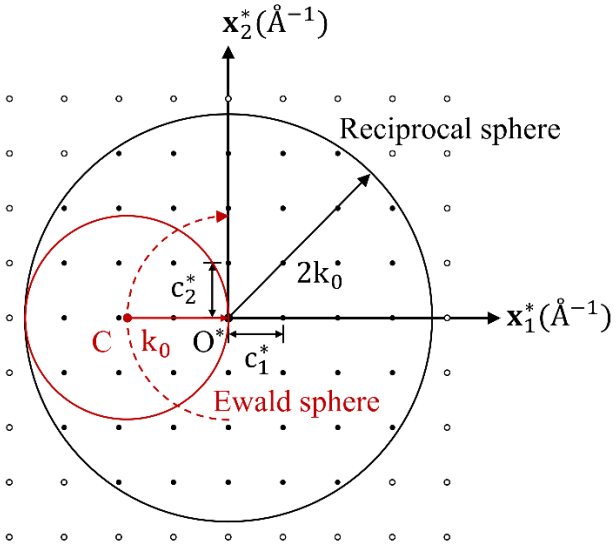

Figure 1. Schematic for X-ray diffraction or neutron diffraction

3.3 Electron diffraction

Electrons are charged particles with a mass approximately 1/2000 of that of photons or neutrons. As a result, electrons have susceptibility to electric fields, relativistic effects, and more importantly, a de Broglie wavelength on the order of 10^{-2}Å, e.g., 0.0251Å (corresponding to an accelerating voltage of 200 kV). Such small wavelength leads to a large radius of the Ewald sphere and high probability of atomic scattering. The interaction between incident electrons and sample atoms involves elastic scattering (by atomic nuclei) and inelastic scattering (by electrons outside the nucleus).

Electron diffraction is primarily applied in Transmission Electron Microscopy (TEM), Scanning Electron Microscopy (SEM), and Electron Back-Scattered Diffraction (EBSD) for structure, composition, and orientation analyses. The diffraction produces diffraction patterns, among which spot patterns are used to

determine second phases, twin structures, orientation relationships, and etc., while Kikuchi patterns provide information on crystalline structures, phase transitions, precise determination of crystal orientation, and etc.

3.3.1 Kinematic electron diffraction

The calculation of the electron diffraction intensity $I_e(\mathbf{g})$ is derived from the Schrödinger equation, as follows [9]:

First, the scattering of high-energy electrons can be described by the Schrödinger equation including relativistic effects:

$$\Delta\Psi + 4\pi^2 \mathrm{k}_0^2 \Psi = -4\pi^2 U(\mathbf{r})\Psi \tag{3.3.1}$$

$$U(\mathbf{r}) \equiv \frac{2me}{h^2} V(\mathbf{r}) = \frac{\sigma}{\pi\lambda} V(\mathbf{r})$$

Here, k_0 is the relativistic wavenumber, and $\mathrm{k}_0 \equiv \frac{\sqrt{2me\Phi}}{h}$ with Φ being the relativistic acceleration potential related to E; σ is the interaction constant given by $\sigma \equiv \frac{2\pi me\lambda}{h^2}$; m is the relativistic electron mass given by $m = m_0\gamma$ and $\gamma = 1 + \frac{eE}{m_0 c^2}$ (m_0 is the rest mass of the electron, e is the electron charge, c is the speed of light, and h is Planck's constant); $V(\mathbf{r})$ is the electrostatic lattice potential.

Next, $V(\mathbf{r}) = V(\mathbf{r}) + \mathrm{i}W(\mathbf{r})$ can be reformulated through the Fourier transformation, i.e., $f(\mathbf{r}) = \mathcal{F}^{-1}[f(\mathbf{g})] \equiv \iiint f(\mathbf{g})\mathrm{e}^{2\pi\mathrm{i}\mathbf{g}\cdot\mathbf{r}}\mathrm{d}\mathbf{g}$, as below:

$$V(\mathbf{r}) = V_0 + V'^{(\mathbf{r})} + \mathrm{i}W(\mathbf{r}) = V_0 + \sum_{\mathbf{g}\neq 0} V_{\mathbf{g}}\mathrm{e}^{2\pi\mathrm{i}\mathbf{g}\cdot\mathbf{r}} + \sum_{\mathbf{g}} W_{\mathbf{g}}\mathrm{e}^{2\pi\mathrm{i}\mathbf{g}\cdot\mathbf{r}} \tag{3.3.2}$$

where V_0 is the positive mean inner potential; $V_{\mathbf{g}}$ and $W_{\mathbf{g}}$ are Fourier coefficients that describe the elastic and inelastic scattering of electrons, respectively, and can be calculated using Weickenmeier-Kohl formula [10]. Thus, the equation (3.3.1) is

rewritten as：

$$\Delta\Psi + 4\pi^2 \mathrm{k}_0^2 \Psi = -4\pi^2 [U + iU']\Psi \tag{3.3.3}$$

$$U(\mathbf{r}) = \frac{2me}{h^2} \sum_{\mathbf{g}\neq 0} V_{\mathbf{g}} \mathrm{e}^{2\pi i \mathbf{g}\cdot\mathbf{r}}$$

$$U'(\mathbf{r}) = \frac{2me}{h^2} \sum_{\mathbf{g}} W_{\mathbf{g}} \mathrm{e}^{2\pi i \mathbf{g}\cdot\mathbf{r}}$$

Here, $\mathrm{k}_0 \equiv \frac{\sqrt{2me\widehat{\Psi}_c}}{h}$ and $\widehat{\Psi}_c = \widehat{\Psi} + \gamma V_0$ $(\gamma = 1 + \frac{eE}{m_0 c^2})$.

Finally, $I_e(\mathbf{g})$ is calculated using kinematic and dynamic theories: The kinematic theory assumes that there is no interaction between the incident and diffracted waves, and the scattering occurs only once without absorption effects, so $I_e(\mathbf{g})$ is proportional to the $\left|V_{\mathbf{g}}\right|^2$; The dynamical theory considers the interaction between the incident and diffracted waves, as well as the multiple scattering and absorption effects, so the solution to the equation (3.3.3) is required.

The search for the reciprocal vectors $\mathbf{g}$ is limited to the slice that is perpendicular to the incident beam $\mathbf{k}_0$ and intersects with the Ewald sphere. The partial reciprocal points in the slice deviate from the Ewald sphere in varying extents, as shown in Fig. 2a. According to the Ewald diagram, only the reciprocal points $\mathbf{g}$ that lie on the Ewald sphere satisfy the Bragg's condition. However, due to the large k_0, the sphere surface inside the slice can be approximated as a plane, which directly produces a diffraction pattern.

The Kikuchi patterns are generated based on the reciprocal points $\mathbf{g}$ and the corresponding diffraction intensity $I_e(\mathbf{g})$. Figure 2b displays that Kikuchi lines are the intersection between the Kossel cone with $\mathbf{g}$ as the central axis, θ as the

inclination angle, and the Kikuchi sphere. Their intensities are equal to the diffraction intensity $I_e(\mathbf{g})$. The Kossel cone originates from the Bragg's diffraction occurring on the same plane induced by inelastically scattered electrons with different scattering directions. Kikuchi diffraction has the following characteristics: the Kikuchi lines are close to straight lines because of small diffraction angle 2θ; the Kikuchi lines emerge in pairs and form the Kikuchi bands, since each (hkl) plane has corresponding $(\bar{h}\bar{k}\bar{l})$ one.

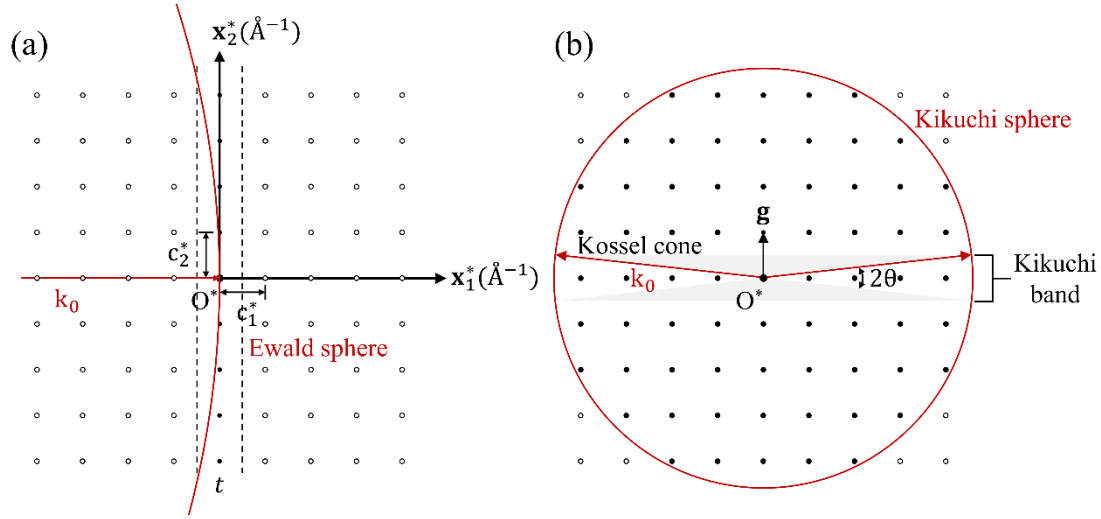

Figure 2. Schematic for kinematic electron diffraction

3.3.2 Dynamical electron diffraction

The dynamical electron diffraction intensity $I_e(\mathbf{g})$ is calculated from the Schrödinger equation (3.3.3), which includes relativistic effects and Fourier transformation. Thus, it is necessary to discuss two expansions of the wave function $\Psi(\mathbf{r})$:

Under the Bragg's condition, where the electrons move only along $\mathbf{k}_0$ and $\mathbf{k}_1 = \mathbf{k}_0 + \mathbf{g}$, the $\Psi(\mathbf{r})$ is expanded as a series of plane waves:

$$\Psi(\mathbf{r}) = \sum_{\mathbf{g}} \phi_{\mathbf{g}} e^{2\pi \mathrm{i}(\mathbf{k}_0+\mathbf{g})\cdot\mathbf{r}} \tag{3.3.4}$$

where $\phi_{\mathbf{g}}$ is the amplitude of a plane wave (or diffracted wave) $\mathbf{k}_0 + \mathbf{g}$, and $\mathbf{g}$ is the reciprocal point on the surface of Ewald sphere. Assuming that an arbitrary reciprocal point is represented by $\mathbf{g}' - \mathbf{g}$, where $\mathbf{g}'$ indicates the reciprocal point not on the surface of Ewald sphere. Under the high-energy approximation and perfect crystal assumption, the Schrödinger equation (3.3.3) can be transformed into the following equation, which describes the variation of the $\phi_{\mathbf{g}}$ with the sample depth z:

$$\frac{d\phi_{\mathbf{g}}}{dz} - 2\pi \mathrm{i} s_{\mathbf{g}} \phi_{\mathbf{g}} = \mathrm{i}\pi \sum_{\mathbf{g}'} \frac{\mathrm{e}^{\mathrm{i}\theta_{\mathbf{g}-\mathbf{g}'}}}{q_{\mathbf{g}-\mathbf{g}'}} \phi_{\mathbf{g}'} \tag{3.3.5}$$

$$s_{\mathbf{g}} \equiv \frac{k_0^2 - (\mathbf{k}_0+\mathbf{g})^2}{2|\mathbf{k}_0+\mathbf{g}|\cos\alpha}$$

$$\frac{1}{q_{\mathbf{g}}} \equiv \frac{1}{\xi_{\mathbf{g}}} + \mathrm{i}\frac{e^{\mathrm{i}\beta_{\mathbf{g}}}}{\xi'_{\mathbf{g}}}$$

where $s_{\mathbf{g}}$ is the excitation error evaluating the deviation between the reciprocal point and the Ewald sphere along the $\mathbf{e}_z$ direction, i.e., sample normal; α is the angle between $\mathbf{k}_0 + \mathbf{g}$ and $\mathbf{e}_z$; $\beta_{\mathbf{g}} = \theta'_{\mathbf{g}} - \theta_{\mathbf{g}}$, where $\theta_{\mathbf{g}}$ and $\theta'_{\mathbf{g}}$ are the phases of $U_{\mathbf{g}}$ and $U'_{\mathbf{g}}$, respectively; $\xi_{\mathbf{g}}$ is the extinction distance, and $\xi'_{\mathbf{g}}$ is the absorption length:

$$\frac{1}{\xi_{\mathbf{g}}} \equiv \frac{|U_{\mathbf{g}}|}{|\mathbf{k}_0+\mathbf{g}|\cos\alpha}, \frac{1}{\xi'_{\mathbf{g}}} \equiv \frac{|U'_{\mathbf{g}}|}{|\mathbf{k}_0+\mathbf{g}|\cos\alpha} \tag{3.3.6}$$

Not imposing the Bragg's condition, the wave function $\Psi(\mathbf{r})$ can be transformed into the following Bloch waves:

$$\Psi(\mathbf{r}) = \sum_{\mathbf{g}} C_{\mathbf{g}}\, \mathrm{e}^{2\pi \mathrm{i}(\mathbf{k}+\mathbf{g})\cdot\mathbf{r}} \tag{3.3.7}$$

where $\mathbf{k}$ is the Bloch wave vector, and $C_{\mathbf{g}}$ are the Bloch wave coefficients. By

substituting the Bloch waves into the equation (3.3.3), the dispersion relation between the Bloch wave vector $\mathbf{k}$ and the incident electron energy (represented by k_0) can be constructed:

$$[k_0^2 - (\mathbf{k}+\mathbf{g})^2]C_{\mathbf{g}} + \sum_{\mathbf{h}\neq\mathbf{g}} U_{\mathbf{g}-\mathbf{h}} C_{\mathbf{h}} = 0 \tag{3.3.8}$$

Under the N-beam condition and considering absorption effects, there are $2N$ Bloch wave vectors $\mathbf{k}^{(j)} = \mathbf{k}_0 + \Gamma^{(j)}\mathbf{n}$, where $\Gamma^{(j)} = \gamma^{(j)} + \mathrm{i}q^{(j)}$ and $\mathbf{n} = -\mathbf{e}_z$. The wave function $\Psi(\mathbf{r})$ can be further transformed into:

$$\Psi(\mathbf{r}) = \sum_j \alpha^{(j)} \sum_{\mathbf{g}} C_{\mathbf{g}}^{(j)} \mathrm{e}^{2\pi\mathrm{i}(\mathbf{k}^{(j)}+\mathbf{g})\cdot\mathbf{r}} \tag{3.3.9}$$

where $\alpha^{(j)}$ is the excitation amplitude of the j-th Bloch wave. By combining the plane wave expansion of $\Psi(\mathbf{r})$ under the Bragg's condition, it can be deduced that $\alpha^{(j)}$ is the inverse matrix of $C^{(j)}$. Under the high-energy approximation, only forward scattering is considered, thus N Bloch wave vectors are regarded. The above dispersion relation can be rewritten as follows:

$$2k_0 s_{\mathbf{g}} C_{\mathbf{g}}^{(j)} + \sum_{\mathbf{h}\neq\mathbf{g}} U_{\mathbf{g}-\mathbf{h}} C_{\mathbf{h}}^{(j)} = 2k_n \Gamma^{(j)} C_{\mathbf{g}}^{(j)} \tag{3.3.10}$$

It is equivalent to the following eigenvalue equation：

$$\begin{pmatrix} \mathrm{i}U_0' & U_{-\mathbf{g}} + \mathrm{i}U_{-\mathbf{g}}' & \cdots & U_{-\mathbf{h}} + \mathrm{i}U_{-\mathbf{h}}' \\ U_{\mathbf{g}} + \mathrm{i}U_{\mathbf{g}}' & 2k_0 s_{\mathbf{g}} + \mathrm{i}U_0' & \cdots & U_{\mathbf{g}-\mathbf{h}} + \mathrm{i}U_{\mathbf{g}-\mathbf{h}}' \\ \vdots & \vdots & \ddots & \vdots \\ U_{\mathbf{h}} + \mathrm{i}U_{\mathbf{h}}' & U_{\mathbf{h}-\mathbf{g}} + \mathrm{i}U_{\mathbf{h}-\mathbf{g}}' & \cdots & 2k_0 s_{\mathbf{h}} + \mathrm{i}U_0' \end{pmatrix} \begin{pmatrix} C_0^{(j)} \\ C_{\mathbf{g}}^{(j)} \\ \vdots \\ C_{\mathbf{h}}^{(j)} \end{pmatrix} = 2k_n \Gamma^{(j)} \begin{pmatrix} C_0^{(j)} \\ C_{\mathbf{g}}^{(j)} \\ \vdots \\ C_{\mathbf{h}}^{(j)} \end{pmatrix} \tag{3.3.11}$$

where $\mathrm{k}_n = \mathbf{n}\cdot\mathbf{k}_0$. The equation defines the interaction between strong diffracted waves $\mathbf{g}$. If the interaction between the weak diffracted waves $\mathbf{g}'$ ($|s_{\mathbf{g}}| \gg \lambda|U_{\mathbf{g}}|$) and the strong diffracted waves $\mathbf{g}$ is taken into account, the following equation can be

obtained

$$\begin{pmatrix} \bar{\eta}_0^{(j)} + \mathrm{i}\bar{U}_0' & \bar{U}_{-\mathbf{g}} + \mathrm{i}\bar{U}_{-\mathbf{g}}' & \cdots & \bar{U}_{-\mathbf{h}} + \mathrm{i}\bar{U}_{-\mathbf{h}}' \\ \bar{U}_{\mathbf{g}} + \mathrm{i}\bar{U}_{\mathbf{g}}' & \bar{\eta}_{\mathbf{g}}^{(j)} + \mathrm{i}\bar{U}_0' & \cdots & \bar{U}_{\mathbf{g}-\mathbf{h}} + \mathrm{i}\bar{U}_{\mathbf{g}-\mathbf{h}}' \\ \vdots & \vdots & \ddots & \vdots \\ \bar{U}_{\mathbf{h}} + \mathrm{i}\bar{U}_{\mathbf{h}}' & \bar{U}_{\mathbf{h}-\mathbf{g}} + \mathrm{i}\bar{U}_{\mathbf{h}-\mathbf{g}}' & \cdots & \bar{\eta}_{\mathbf{h}}^{(j)} + \mathrm{i}\bar{U}_0' \end{pmatrix} \begin{pmatrix} C_0^{(j)} \\ C_{\mathbf{g}}^{(j)} \\ \vdots \\ C_{\mathbf{h}}^{(j)} \end{pmatrix} = 0 \tag{3.3.12}$$

$$\bar{U}_{\mathbf{g}-\mathbf{h}} \equiv U_{\mathbf{g}-\mathbf{h}} - \sum_{\mathbf{h}'} \frac{U_{\mathbf{g}-\mathbf{h}'} U_{\mathbf{h}'-\mathbf{h}}}{\eta_{\mathbf{h}'}^{(j)}}$$

$$\bar{\eta}_{\mathbf{g}}^{(j)} \equiv \eta_{\mathbf{g}}^{(j)} - \sum_{\mathbf{h}'} \frac{\left|U_{\mathbf{g}-\mathbf{h}'}\right|^2}{\eta_{\mathbf{h}'}^{(j)}}$$

Here, $\eta_{\mathbf{g}}^{(j)} \equiv 2\left[\mathrm{k}_0 s_{\mathbf{g}} - k_n \Gamma^{(j)}\right]$. The Bloch wave excitation amplitude $\alpha^{(j)}$ and Bloch wave coefficients $C_{\mathbf{g}}^{(j)}$ can be solved based on the equation.

Based on the probability interpretation, the intensity contribution $I_e(\mathbf{g})$ from a single wave vector $\mathbf{k} = \mathbf{k}_0 + \mathbf{g}$ is proportional to $\left|\phi_{\mathbf{g}}\right|^2$, and $\phi_{\mathbf{g}}$ is calculated as[11]:

$$\phi_{\mathbf{g}}(z_0) = \sum_j^{N_{\mathbf{g}}} \alpha^{(j)} C_{\mathbf{g}}^{(j)}\, \mathrm{e}^{2\pi \mathrm{i}\Gamma^{(j)} \cdot z_0} \tag{3.3.13}$$

where z_0 is the sample thickness. The intensity contribution $I_e(\mathbf{k}_0)$ from an incident beam $\mathbf{k}_0$ is proportional to $|\Psi(\mathbf{r})|^2$, and calculated as:

$$I_e(\mathbf{k}_0) = \frac{1}{z_0} \int_0^{z_0} \Psi^*(\mathbf{r}) \Psi(\mathbf{r})\, \mathrm{d}z = \sum_{\mathbf{g}} \sum_{\mathbf{h}} S_{\mathbf{gh}} L_{\mathbf{gh}} \tag{3.3.14}$$

Here, $S_{\mathbf{gh}}$ describes the interaction between the incident and diffracted waves:

$$S_{\mathbf{gh}} \equiv \sum_n^N \sum_{i \epsilon S_n} Z_n^2 \mathrm{e}^{-M_{\mathbf{h}-\mathbf{g}}^{(n)}} \mathrm{e}^{2\pi \mathrm{i}(\mathbf{h}-\mathbf{g}) \cdot \mathbf{r}_i} \tag{3.3.15}$$

Here, Z_n is the atomic number of the equivalent atomic group S_n, and $\mathrm{e}^{-M_{\mathbf{h}-\mathbf{g}}^{(n)}}$ is the temperature factor ($M_{\mathbf{h}-\mathbf{g}}^{(n)} = dw_n(\frac{\mathbf{h}-\mathbf{g}}{2})^2$); $L_{\mathbf{gh}}$ describes multiple scattering and absorption effects as the incident wave passes through the target sample:

$$L_{\mathbf{gh}} \equiv \sum_j \sum_k C_{\mathbf{g}}^{(j)*} \alpha^{(j)*} \mathcal{M}_{jk} \alpha^{(k)} C_{\mathbf{h}}^{(k)} \tag{3.3.16}$$

$\mathcal{M}_{jk}$ is calculated as:

$$\mathcal{M}_{jk} \equiv \frac{1}{z_0}\int_0^{z_0} \mathrm{e}^{-2\pi(\alpha_{jk}+\mathrm{i}\beta_{jk})z}\mathrm{d}z \tag{3.3.17}$$

$$\alpha_{jk} = q^{(j)} + q^{(k)}$$

$$\beta_{jk} = \gamma^{(j)} - \gamma^{(k)}$$

The above calculation assumes that the scattered electrons are uniformly distributed along the $\mathbf{e}_z$ direction. For simulating EBSD condition, the energy, depth, and directional distributions of back-scattered electrons is obtained through Monte Carlo (MC) simulations [12]. Figure 3 shows that each incident electron repeatedly undergoes random movement and random scattering in the sample. The electron energy follows the CSDA approximation (Continuous Slowing Down Approximation, where the electron energy E_i only depends on the mean free path length $|\boldsymbol{s}_i|$), until the energy loss exceeds the preset value or the electron exits the sample. In this case, the equation (3.3.17) can be modified as:

$$\mathcal{M}_{jk}(E) \equiv \frac{1}{z(E)}\int_0^{z(E)} \lambda(E,z)\mathrm{e}^{-2\pi(\alpha_{jk}+\mathrm{i}\beta_{jk})z}\mathrm{d}z \tag{3.3.18}$$

$z(E)$ and $\lambda(E,z)$ are integral depth and scattering probability of backscattered electrons.

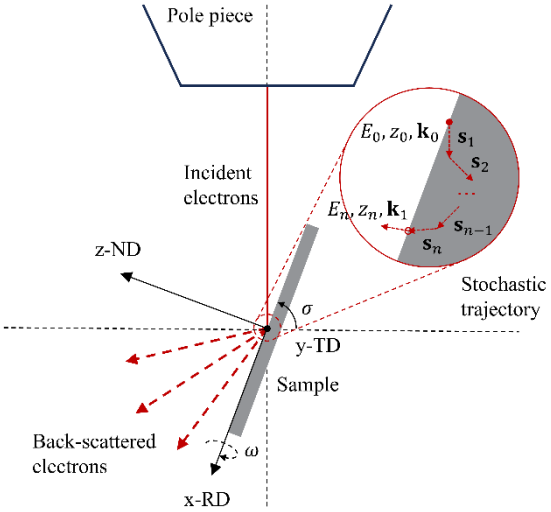

Figure 3. Schematic for the Monte Carlo simulation of back-scattered electrons

3.4 Structural analysis

The radial distribution function and the static structure factor are commonly used for structural analyses. The radial distribution function is the ratio between the probability of j atoms within a spherical shell of thickness Δr, distance r from an i atom, and the probability of j atoms throughout the entire simulation cell. Its formula is as follows:

$$g_{ij}(r) = \frac{1}{\rho_j} \frac{\sum_i^{N_i} n_{ij}(r)}{N_i V(r)} \tag{3.4.1}$$

Here, ρ_j is the density of j atoms; $n_{ij}(r)$ is the number of j atoms within the spherical shell at a distance between $r - \frac{1}{2}\Delta r$ and $r + \frac{1}{2}\Delta r$ from the i atom; $V(r) = \frac{4}{3}\pi\left(r + \frac{1}{2}\Delta r\right)^3 - \frac{4}{3}\pi\left(r - \frac{1}{2}\Delta r\right)^3$. The $g_{ij}(r)$ profile offers a series of structural parameters: the average nearest-neighbor distance, which corresponds to the location of the first peak; the glass transition temperature, which is empirically determined by the ratio of the first minimum and the first maximum [13]; and so on.

The general formula for the static structure factor is as follows [14]:

$$S_{ij}(\mathbf{q}) = \frac{1}{N}\langle \sum_{i=1}^{N_i} e^{\mathrm{i}\mathbf{q}\cdot\mathbf{r}_i} \sum_{j=1}^{N_j} e^{-\mathrm{i}\mathbf{q}\cdot\mathbf{r}_j} \rangle \tag{3.4.2}$$

Here, the increment of the wave vector $\mathbf{q}$ is $\Delta\mathbf{q} = (2\pi/L_x, 2\pi/L_y, 2\pi/L_z)$, where L_x, L_y, and L_z are the dimensions of the simulation cell constrained by periodic boundary conditions. By averaging $S_{ij}(\mathbf{q})$ with the same q, $S_{ij}(\mathrm{q})$ is obtained. Additionally, the $S_{ij}(\mathrm{q}) - 1$ can be obtained through the Fourier transformation of $g_{ij}(r) - 1$:

$$S_{ij}(\mathrm{q}) - 1 = 4\pi \int_0^{\infty} \frac{\sin(qr)}{qr} \left[g_{ij}(r) - 1\right] r^2 \, dr \tag{3.4.3}$$

Similarly, The $S_{ij}(\mathrm{q})$ profile provides a series of structural information: the classification of liquid metals; the Hansen-Verlet freezing criterion [15]; and so on.

4 Syntax and functionality

The section will introduce the basic usages of AAVDP, which currently includes diffraction simulations, structural analyses, and etc. The general syntax and rules of AAVDP are as follows:

General Syntax:

AAVDP <--mode> (inputfile) <-option> [value]

Description:

In the general command-line format, --mode represents the diffraction/analysis mode, such as --xrd, --scherrer, --ked, and --gauss; inputfile refers to the model file in LAMMPS or VASP format; -option represents the parameters required by the

diffraction/analysis mode and value indicates the specific value, e.g., -e specifies the atomic types of the model file and -l specifies the wavelength λ of the incident wave.

4.1 X-ray Diffraction (XRD)

Mode: xrd

Syntax:

AAVDP --xrd [inputfile] -e [type1] [type2] … [typeN] -dw [DW1] [DW2] … [DWN] -l [lambda] -2t [2theta_min] [2theta_max] -lp [Lorentz_polarization_type] -c [c1] [c2] [c3] -auto/manu -thr [threshold] -o [outputfile] --scherrer -m [mixing_parameter] -d [grain_diameter] -d2t [2theta_bin]

Description:

This mode is used to simulate the diffraction phenomena as incident X-rays interact with the sample. As a model file in either LAMMPS Data format or VASP format is input, data including diffraction angles, diffraction intensities, normalized diffraction intensities, and corresponding diffraction image are outputted:

- -e and -dw: -e specifies N atomic types in the model file referring to the 211 elements (H-Cf) and ions at the Atomic form factors (tugraz.at) website, which can be ignored if atomic types are included in the file. -dw specifies the corresponding Debye-Waller factors with defaults as $0.0\,\text{Å}^2$, indicating no calculation of temperature factor.
- -l: specifies the wavelength λ of the incident wave, defaulting to 1.54184 Å.
- -2t: specifies the minimum and maximum of diffraction angles 2θ, defaulting to

0° and 90°, respectively.

- -lp: specifies the calculation type of Lorentz-polarization factor, in which 0 means no calculation of Lorentz-polarization factor, 1 means the calculation of only polarization factor, 2 means the calculation of Lorentz-polarization factor for small crystals, and 3 means the calculation of Lorentz-polarization factor for polycrystals with random grain orientations. The default calculation type is 3.
- -c and -auto/manu: -c specifies three reciprocal spacings in the reciprocal mesh. -auto indicates automatically setting three reciprocal spacings as the inverse of the three simulation dimensions with scaling factors c_1, c_2, and c_3, all defaulting to 1.0. -manu indicates manually setting three reciprocal spacings as c_1, c_2, and c_3, with a default value of 0.1Å^{-1}. The former mode is automatically activated.
- -thr: specifies the threshold of diffraction intensity with a default value of 0.001, meaning that diffraction intensities below 0.001 times the maximum diffraction intensity will be ignored when outputting.
- -o: specifies the path of diffraction data file, defaulting to ./AAVDP.xrd. The corresponding diffraction image will be saved as ./AAVDP.xrd.png.

If --scherrer is specified, the Scherrer smearing of diffraction lines is activated:

- -m: specifies the mixing parameter η for the pseudo-Voigt function (3.2.6). 0 represents a pure Gaussian, 1 represents a pure Lorentzian, and the value between 0 and 1 represents a Gaussian-Lorentz mixture. The default is 0.
- -d: specifies the grain diameter in the Scherrer equation (3.2.7), defaulting to 500 Å.

- -d2t: specifies the bin of diffraction angle 2θ, defaulting to 0.01°.

4.2 Neutron Diffraction (NED)

Mode: ned

Syntax:

AAVDP --ned [inputfile] -e [type1] [type2] … [typeN] -dw [DW1] [DW2] … [DWN] -l [lambda] -2t [2theta_min] [2theta_max] -lp [Lorentz_type] -c [c1] [c2] [c3] -auto/manu -thr [threshold] -o [outputfile] --scherrer -m [mixing_parameter] -d [grain_diameter] -d2t [2theta_bin]

Description:

This mode is used to simulate the diffraction phenomena as incident neutrons interact with the sample. As a model file in either LAMMPS Data format or VASP format is input, data including diffraction angles, diffraction intensities, normalized diffraction intensities, and corresponding diffraction image are outputted:

- -e and -dw: -e specifies N atomic types in the model file referring to the 336 elements (H-Cm) and ions at the Neutron scattering lengths and cross sections (nist.gov) website, which can be ignored if atomic types are included in the file. -dw specifies the corresponding Debye-Waller factors with defaults as 0.0$Å^2$, indicating no calculation of temperature factor.
- -l: specifies the wavelength λ of the incident wave, defaulting to 1.54184 Å.
- -2t: specifies the minimum and maximum of diffraction angles 2θ, defaulting to $0°$ and $90°$, respectively.

- -lp: specifies the calculation type of Lorentz factor, in which 0 means no calculation of Lorentz factor, 1 means the calculation of Lorentz factor for small crystals, and 2 means the calculation of Lorentz factor for polycrystals with random grain orientations. The default calculation type is 2.
- -c and -auto/manu: -c specifies three reciprocal spacings in the reciprocal mesh. -auto indicates automatically setting three reciprocal spacings as the inverse of the three simulation dimensions with scaling factors c_1, c_2, and c_3, all defaulting to 1.0. -manu indicates manually setting three reciprocal spacings as c_1, c_2, and c_3, with a default value of 0.1Å^{-1}. The former mode is automatically activated.
- -thr: specifies the threshold of diffraction intensity with a default value of 0.001, meaning that diffraction intensities below 0.001 times the maximum diffraction intensity will be ignored when outputting.
- -o: specifies the path of diffraction data file, defaulting to ./AAVDP.ned. The corresponding diffraction image will be saved as ./AAVDP.ned.png.

If --scherrer is specified, the Scherrer smearing of diffraction lines is activated:

- -m: specifies the mixing parameter η for the pseudo-Voigt function (3.2.6). 0 represents a pure Gaussian, 1 represents a pure Lorentzian, and the value between 0 and 1 represents a Gaussian-Lorentz mixture. The default is 0.
- -d: specifies the grain diameter in the Scherrer equation (3.2.7), defaulting to 500 Å.
- -d2t: specifies the diffraction angle bin, with a default value of 0.01°.

4.3 Kinematic Electron Diffraction (KED)

Mode: ked

Syntax:

AAVDP --ked [inputfile] -e [type1] [type2] … [typeN] -dw [DW1] [DW2] … [DWN] -en [voltage] -z [z_1] [z_2] [z_3] -q [qmax] -t [intersection_thickness] -c [c1] [c2] [c3] -auto/manu -thr [threshold] -o [outputfile] --gauss -sig [standard_deviation] -dx [qx_bin] --rotate -x [x_1] [x_2] [x_3] -y [y_1] [y_2] [y_3]

Description:

This mode is used to simulate the kinematic diffraction phenomena as incident electrons interact with the sample. As a model file in either LAMMPS Data format or VASP format is input, data including diffraction vectors, diffraction intensities, normalized diffraction intensities, and corresponding diffraction image are outputted:

- -e and -dw: -e specifies N atomic types in the model file referring to the 98 elements (H-Cf), which can be ignored if atomic types are included in the file. -dw specifies the corresponding Debye-Waller factors with defaults as $0.0Å^2$, indicating no calculation of temperature factor.
- -en: specifies the acceleration voltage of the incident electrons. The default value is 200 kV, corresponding to a wavelength of 0.0251Å.
- -q: specifies the maximum modulus of the reciprocal vector to be searched, defaulting to $1.0Å^{-1}$.
- -z: specifies the incident direction of the electron beam, which is also the normal to the intersection plane of Ewald sphere, defaulting to $[001]$.

- -t: specifies the thickness of the intersection plane of Ewald sphere, defaulting to 0.1Å^{-1}.
- -c and -auto/manu: -c specifies three reciprocal spacings in the reciprocal mesh. -auto indicates automatically setting three reciprocal spacings as the inverse of the three simulation dimensions with scaling factors c_1, c_2, and c_3, all defaulting to 1.0. -manu indicates manually setting three reciprocal spacings as c_1, c_2, and c_3, with a default value of 0.1Å^{-1}. The former mode is automatically activated.
- -thr: specifies the threshold of diffraction intensity with a default value of 0.001, meaning that diffraction intensities below 0.001 times the maximum diffraction intensity will be ignored when outputting.
- -o: specifies the path of diffraction data file, defaulting to ./AAVDP.ked. The corresponding diffraction image will be saved as ./AAVDP.ked.png.

  If --gauss is specified, the smearing of diffraction spots is activated.
- -sig: specifies the standard deviation for the Gaussian function, defaulting to 0.01 Å^{-1}.
- -dx: specifies the coordinate bin along the horizontal axis for the diffraction image, which is the same as that along the vertical axis. The default value is 0.005Å^{-1}.

If --rotate is specified, the rotation of diffraction image is activated. If --rotate is not specified, the horizontal axis is aligned with the direction of the nearest-neighbor diffraction spot, and the vertical axis is the normal to the plane formed by the incident direction and the direction of the nearest-neighbor diffraction spot.

- -x and -y: specify directions corresponding to the horizontal and vertical axes of the diffraction image, respectively. The defaults are [100] for the horizontal axis and [010] for the vertical axis.

4.4 Kinematic Kikuchi Diffraction (KKD)

Mode: kkd

Syntax:

AAVDP --kkd [inputfile] -e [type1] [type2] … [typeN] -en [voltage] -q [qmax] -c [c1] [c2] [c3] -auto/manu -thr [threshold] -z [z_1] [z_2] [z_3] -rx [projection_ratiox] -ry [projection_ratioy] -t [Kikuchi_line_thickness] -px [numpx] -py [numpy] -background [background_color] -o [outputfile] --rotate -x [x_1] [x_2] [x_3] -y [y_1] [y_2] [y_3] --scale -i [intensity_min] [intensity_max]

or

AAVDP --kkd [inputfile] -e [type1] [type2] … [typeN] -en [voltage] -q [qmax] -c [c1] [c2] [c3] -auto/manu -thr [threshold] -o [ked3file] --ked3

AAVDP --kkd [ked3file] -z [z_1] [z_2] [z_3] -rx [projection_ratiox] -ry [projection_ratioy] -t [Kikuchi_line_thickness] -px [numpx] -py [numpy] -background [background_color] -o [outputfile] --rotate -x [x_1] [x_2] [x_3] -y [y_1] [y_2] [y_3] --scale -i [intensity_min] [intensity_max]

Description:

This mode is used to simulate the kinematic Kikuchi phenomena as incident electrons interact with the sample. As a model file in either LAMMPS Data format or

VASP format is input, data including pixel number and pixel intensity of the Kikuchi image based on the stereographic projection, and corresponding Kikuchi image are outputted:

- -e and -dw: -e specifies N atomic types in the model file referring to the 98 elements (H-Cf), which can be ignored if atomic types are included in the file. -dw specifies the corresponding Debye-Waller factor with defaults as $0.0Å^2$, indicating no calculation of temperature factor.
- -en: specifies the acceleration voltage of the incident electrons. The default value is 200 kV, corresponding to a wavelength of 0.0251Å.
- -q: specifies the maximum modulus of the reciprocal vector to be searched, defaulting to 1.0 $Å^{-1}$.
- -c and -auto/manu: -c specifies three reciprocal spacings in the reciprocal mesh. -auto indicates automatically setting three reciprocal spacings as the inverse of the three simulation dimensions with scaling factors c_1, c_2, and c_3, all defaulting to 1.0. -manu indicates manually setting three reciprocal spacings as c_1, c_2, and c_3, with a default value of $0.1Å^{-1}$. The former mode is automatically activated.
- -thr: specifies the threshold of diffraction intensity with a default value of 0.001, meaning that diffraction intensities below 0.001 times the maximum diffraction intensity will be ignored when outputting.
- -z: specifies the projection direction, defaulting to [001], respectively.
- -rx and -ry: specify the horizontal and vertical ratios of the Kikuchi sphere projection relative to the entire Kikuchi hemisphere projection, both defaulting to

1.0.

- -t: specifies the thickness of the Kikuchi lines, defaulting to 0.2 $Å^{-1}$.
- -px and -py: specify the number of pixels along the horizontal and vertical axes of the Kikuchi image, which must be odd. The default values are both 501.
- -thr: specifies the threshold of the diffraction intensity for calculating Kikuchi intensities, with a default value of 0.001, meaning that diffraction intensities below 0.001 times the maximum diffraction intensity will be ignored when calculating.
- -background: specifies the background color for the Kikuchi image, with options of black (b) and white (w). The default is black (b).
- -o: specifies the path of Kikuchi data file, defaulting to ./AAVDP.kkd. The corresponding Kikuchi image will be saved as ./AAVDP.kkd.png.

If --rotate is specified, the rotation of Kikuchi image is activated. If --rotate is not specified, the horizontal axis is aligned with the direction perpendicular to z-axis and lying on the same latitude circle as the z-axis, and the vertical axis is aligned with the direction perpendicular to z-axis and lying on the same meridian circle as the z-axis.

- -x and -y: specify directions corresponding to the horizontal and vertical axes of the Kikuchi image, respectively. The defaults are $[100]$ for the horizontal axis and $[010]$ for the vertical axis.

If --scale is specified, the re-coloring of the Kikuchi image is activated. If --scale is not specified, the coloring automatically adopts the maximum and minimum of the Kikuchi intensity.

- -i: specify the minimum and maximum intensities, defaulting to 0.0 and 1000.0, respectively.

If --ked3 is specified, the step-by-step mode is activated. The diffraction data file with a suffix of .ked3 serves as the outputfile in the first step and the inputfile in the second step, defaulting to ./AAVDP.ked3.

4.5 Dynamical Electron Diffraction (DED)

Mode: ded

Syntax:

AAVDP --ded [inputfile] -e [type1] [type2] … [typeN] -dw [DW1] [DW2] ... -en [voltage] -z [z_1] [z_2] [z_3] -q [qmax] -fn [n_1] [n_2] [n_3] -ft [foil_thickness] -bethe [rg_c1] [rg_c2] [rg_c3] [sg_c] -thr [threshold] -o [outputfile] --gauss -sig [standard_deviation] -dx [qx_bin] --rotate -x [x_1] [x_2] [x_3] -y [y_1] [y_2] [y_3]

Description:

This mode is used to simulate the dynamical diffraction phenomena as incident electrons interact with the sample (foil). As a model file in either LAMMPS Data format or VASP format is input, data including diffraction vectors, diffraction intensities, normalized diffraction intensities, and corresponding diffraction image are outputted:

- -e and -dw: -e specifies N atomic types in the model file referring to the 98 elements (H-Cf), which can be ignored if atomic types are included in the file. -dw specifies the corresponding Debye-Waller factor with defaults as 0.0$Å^2$,

indicating no calculation of temperature factor.

- -en: specifies the acceleration voltage of the incident electrons. The default value is 200 kV, corresponding to a wavelength of 0.0251Å.
- -q: specifies the maximum modulus of the reciprocal vector to be searched, defaulting to 1.0$Å^{-1}$.
- -z: specifies the incident direction of the electron beam, which is also the normal to the intersection plane of Ewald sphere, defaulting to [001].
- -fn and -ft: specify the normal and thickness of the sample, defaulting to [001] and 100.0Å, respectively. It is recommended that the former is consistent with the value specified by -z.
- -bethe: specifies the Bethe parameters, which are used to filter diffracted waves and distinguish between strong and weak diffracted waves. The parameters rg_c_1 and rg_c_2 are partition values for $r_{\mathbf{g}}$, in which if $r_{\mathbf{g}}$ is less than rg_c_1, the $\mathbf{g}$ is regarded as the strong wave; if $r_{\mathbf{g}}$ is between rg_c_1 and rg_c_2, the $\mathbf{g}$ is regarded as the weak wave; if $r_{\mathbf{g}}$ is greater than rg_c_2, the $\mathbf{g}$ is too weak to be ignored. rg_c_3 is the truncate value of $r_{\mathbf{g}}$. $rg\_c_1 < rg\_c_2 < rg\_c_3$, defaulting to 4.0, 8.0, and 50.0, respectively. rg_c is the truncate value for $s_{\mathbf{g}}$, with a default value of 1.0.
- -thr: specifies the threshold of diffraction intensity with a default value of 0.001, meaning that diffraction intensities below 0.001 times the maximum diffraction intensity will be ignored when outputting.
- -o: specifies the path of diffraction data file, defaulting to ./AAVDP.ded. The corresponding diffraction image will be saved as ./AAVDP.ded.png.

If --gauss is specified, the smearing of diffraction spots is activated.

- -sig: specifies the standard deviation for the Gaussian function, defaulting to 0.01 $Å^{-1}$.
- -dx: specifies the coordinate bin along the horizontal axis for the diffraction image, which is the same as that along the vertical axis. The default value is 0.005$Å^{-1}$.

If --rotate is specified, the rotation of diffraction image is activated. If --rotate is not specified, the horizontal axis is aligned with the direction of the nearest-neighbor diffraction spot, and the vertical axis is the normal to the plane formed by the incident direction and direction of the nearest-neighbor diffraction spot:

- -x and -y: specify directions corresponding to the horizontal and vertical axes of the diffraction image, respectively. The defaults are $[100]$ for the horizontal axis and $[010]$ for the vertical axis.

4.6 Dynamical Kikuchi Diffraction (DKD)

Mode: dkd

Syntax:

AAVDP --dkd [inputfile] -e [type1] [type2] … [typeN] -dw [DW1] [DW2] … [DWN] -en [voltage] -q [qmax] -ft [foil_thickness] -bethe [rg_c1] [rg_c2] [rg_c3] [sg_c] -z [z_1] [z_2] [z_3] -rx [projection_ratiox] -ry [projection_ratioy] -px [numpx] -py [numpy] -background [background_color] -o [outputfile] --monte -rd [rotation_angle] -td [tilt_angle] -ex [energy_exit] -dt [foil_depth_bin] -ne [nume] -np [nump] -seed

[randomfile] -o [outputfile] --rotate -x [x_1] [x_2] [x_3] -y [y_1] [y_2] [y_3] --scale -i [intensity_min] [intensity_max]

Description:

This mode is used to simulate the dynamical Kikuchi phenomena as incident electrons interact with the sample (foil). As a model file in either LAMMPS Data format or VASP format is input, data including pixel number and pixel intensity of the Kikuchi image based on the stereographic projection, and corresponding Kikuchi image are outputted:

- -e and -dw: -e specifies N atomic types in the model file referring to the 98 elements (H-Cf), which can be ignored if atomic types are included in the file. -dw specifies the corresponding Debye-Waller factors with defaults as 0.0Å^2, indicating no calculation of temperature factor.
- -en: specifies the acceleration voltage of the incident electrons. The default value is 200 kV, corresponding to a wavelength of 0.0251Å.
- -q: specifies the maximum modulus of the reciprocal vector to be searched, defaulting to 1.0Å^{-1}.
- -ft: specifies the thickness of the sample, defaulting to 100.0Å.
- -bethe: specifies the Bethe parameters, which are used to filter diffracted waves and distinguish between strong and weak diffracted waves. The parameters rg_c_1 and rg_c_2 are partition values for $r_{\mathbf{g}}$, in which if $r_{\mathbf{g}}$ is less than rg_c_1, the $\mathbf{g}$ is regarded as the strong wave; if $r_{\mathbf{g}}$ is between rg_c_1 and rg_c_2, the $\mathbf{g}$ is regarded as the weak wave; if $r_{\mathbf{g}}$ is greater than rg_c_2, the $\mathbf{g}$ is too weak to be ignored.

rg_c_3 is the truncate value of $r_{\mathbf{g}}$. rg_c_1 < rg_c_2 < rg_c_3, defaulting to 4.0, 8.0, and 50.0, respectively; rg_c is the truncate value for $s_{\mathbf{g}}$, with a default value of 1.0.

- -z: specifies the projection direction, defaulting to [001].
- -rx and -ry: specify the horizontal and vertical ratios of the Kikuchi sphere projection relative to the entire Kikuchi hemisphere projection, both defaulting to 1.0.
- -px and -py: specify the number of pixels along the horizontal and vertical axes of the Kikuchi image, which must be odd. The default values are both 501.
- -background: specifies the background color for the Kikuchi image, with options of black (b) and white (w). The default is black (b).
- -o: specifies the path of Kikuchi data file, defaulting to ./AAVDP.dkd. The corresponding Kikuchi image will be saved as ./AAVDP.dkd.png.

If --monte is specified, the Monte Carlo (MC) simulation for the energy, spatial, and directional distributions of backscattered electrons is activated. The Lambert projection image of the backscattered electrons distribution on the directional hemisphere is generated.

- -rd and -td: -ome specifies the rotation angle of the sample along the rolling direction (RD), defaulting to 0.0°. -sig specifies the tilt angle of the sample along the transverse direction (TD), defaulting to 75.7°.
- -ex: specifies the minimum electron energy during the MC simulation, which must be less than the acceleration voltage of the incident electrons (corresponding to the maximum electron energy). The default value is 190 kV.

- -dt: specifies the depth bin of electron incidence into the sample, which must be less than the sample thickness (corresponding to the maximum depth of electron incidence into the sample). The default value is 10Å.
- -ne: specifies the number of incident electrons, defaulting to 20000.
- -np: specifies the number of pixels along the edge of the projection image, which must be odd. The default value is 501.
- -seed: specifies the path of random seed file, defaulting to ./RandomSeeds.data, which is currently stored in the AAVDP folder.
- -o: specifies the path of projection data file, defaulting to ./AAVDP.mc. The corresponding projection image will be saved as ./AAVDP.mc.png.

If --rotate is specified, the rotation of Kikuchi image is activated. If --rotate is not specified, the horizontal axis is aligned with the direction perpendicular to z-axis and lying on the same latitude circle as the z-axis, and the vertical axis is aligned with the direction perpendicular to z-axis and lying on the same meridian circle as the z-axis.

- -x and -y: specify directions corresponding to the horizontal and vertical axes of the Kikuchi image, respectively. The defaults are [100] for the horizontal axis and [010] for the vertical axis.

If --scale is specified, the re-coloring of the Kikuchi image is activated. If --scale is not specified, the coloring automatically adopts the maximum and minimum of the Kikuchi intensity.

- -i: specify the minimum and maximum intensities, defaulting to 0.0 and 1000.0, respectively.

4.7 Radial Distribution Function (RDF)

Mode: rdf

Syntax:

AAVDP --rdf [inputfile] -r [rmax] -n [nbin] -partial -o [outputfile]

Description:

This mode is used to simulate the radial distribution function. As a model file in LAMMPS Data format or VASP format is input, data including radial distance, radial distribution function, and related images are outputted.

- -r: specifies the maximum radial distance, defaulting to 5.0Å.
- -n: specifies the number of bins for the radial distance, defaulting to 200.
- -partial: activates the calculation of partial distribution functions.
- -o: specifies the path of data file, defaulting to ./AAVDP.rdf. The corresponding images will be saved as ./AAVDP.rdf.i-j.png, where i and j refer to atomic types (or arbitrary atomic type if specified as *).

4.8 Static Structure Factor (SSF)

Mode: ssf

Syntax:

AAVDP --ssf [inputfile] -q [qmax] -n [nbin] -partial -o [outputfile] --rdf -r [rmax] -n [nbin]

Description:

This mode is used to simulate the static structure factor. As a model file in LAMMPS Data format or VASP format is input, data including the magnitude of wave vector, static structure factor and corresponding images are outputted:

- -q: specifies the maximum magnitude of wave vector, defaulting to 5.0 Å.
- -n: specifies the number of bins for the magnitude of wave vector, defaulting to 200.
- -partial: activates the calculation of partial static structure factors.
- -o: specifies the path of data file, defaulting to ./AAVDP.ssf. The corresponding images will be saved as ./AAVDP.ssf.i-j.png, where i and j refer to atomic types (or arbitrary atomic type if specified as *).

If the --rdf is specified, the radial distribution function is used to calculate the static structure factor.

- -r: specifies the maximum radial distance, defaulting to 5.0Å.
- -n: specifies the number of bins for the radial distance, defaulting to 200.

5 Examples

5.1 The XRD for cubic NaCl and hexagonal ZnO

This mode is used to demonstrate the XRD analysis of the AAVDP program using cubic NaCl and hexagonal ZnO as examples. The commands are as follows:

```
>>./bin/AAVDP_win.exe --xrd ./exp/xrd/NaCl/NaCl.vasp -dw 1.72 1.41 -l 1.54056 -2t 20.0 90.0 -o ./exp/xrd/NaCl/NaCl1.xrd
```

```
>>./bin/AAVDP_win.exe --xrd ./exp/xrd/NaCl/NaCl.vasp -dw 1.72 1.41 -l 1.54439 -2t 20.0 90.0 -o ./exp/xrd/NaCl/NaCl2.xrd
>>./bin/AAVDP_win.exe --xrd ./exp/xrd/ZnO/ZnO.vasp -2t 0 80 -o ./exp/xrd/ZnO/ZnO_line.xrd
>>./bin/AAVDP_win.exe --xrd ./exp/xrd/ZnO/ZnO.vasp -2t 0 80 -o ./exp/xrd/ZnO/ZnO.xrd --scherrer -m 0.5 -d 294 -d2t 0.02
```

The selected space group for NaCl is $Fm\bar{3}m$, with a lattice constant of 5.6407Å. The test sample is a powder with a particle size of approximately 45 um. The testing conditions are at room temperature (290K), with X-ray radiation from a copper target's $K\alpha_1$ and $K\alpha_2$ lines. The step size for the diffraction angle is 0.05°. Since the wavelengths of $K\alpha_1$ and $K\alpha_2$ X-rays are different (typically 1.54056Å and 1.54439 Å, respectively), the $I-2\theta$ curve may show a distinct double splitting at high angles. Therefore, the final diffraction intensity is calculated by integrating the intensities of both lines with a 2:1 ratio.

Table 1 shows the comparison between the experimental and calculated diffraction intensities for NaCl. As can be seen, the results provided by AAVDP are in good agreement with the experimental data.

Table 1. Comparison of experimental and calculated diffraction intensities for NaCl

{hkl}	{111}	{200}	{220}	{311}	{222}	{400}	{331}	{420}	{422}
exp.[7]	9.50	100.0	59.57	2.06	17.27	7.05	0.90	17.68	11.18
AAVDP	8.63	100.0	59.74	1.95	17.48	6.97	0.87	16.90	11.42

The selected ZnO has a hexagonal wurtzite structure with the space group

$P6_3mc$. Since the lattice constants are not specified in the literature, the environmental conditions are assumed to be at room temperature for the hexagonal ZnO structure [16], with lattice constants of 3.2500Å and 5.2600Å. The test sample is a nanocrystal with a grain size of approximately 294 nm. The X-ray source is a copper target's Kα line. Since the test conditions are at room temperature, the temperature effect is minimal, and the Debye-Waller factor for oxygen at room temperature has not been clearly defined. Therefore, the calculated diffraction intensity does not account for temperature effects. As shown in **Fig. 4**, it can be observed that the results provided by AAVDP are in good agreement with the experimental data, and the grain size causes the diffraction peaks to broaden.

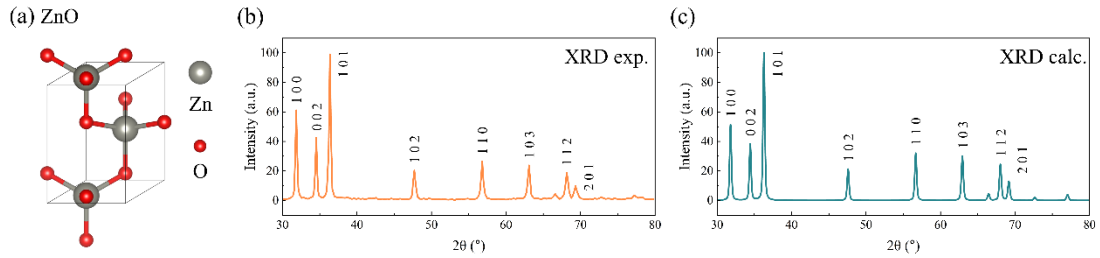

Figure 4. (a) ZnO crystal structure; (b) Experimental XRD pattern of ZnO [16];(c) Simulated XRD pattern of ZnO (AAVDP).

5.2 The NED for cubic FeCo and hexagonal $LaCrGe_3$

This mode demonstrates the NED analysis of the AAVDP program using cubic FeCo and hexagonal $LaCrGe_3$ crystals as examples. The commands are as follows:

```
>>./bin/AAVDP_win.exe --xrd ./exp/xrd/FeCo/FeCo.lmp -e Fe Co -dw 0.5500 0.5500 -2t 0 150 -l 1.5400 -o ./exp/xrd/FeCo/FeCo.xrd
>>./bin/AAVDP_win.exe --xrd ./exp/xrd/FeCo/FeCo_random.lmp -e Fe Co -dw
```

0.5500 0.5500 -2t 0 150 -l 1.5400 -c 10 10 10 -o ./exp/xrd/FeCo/FeCo_random.xrd

>>./bin/AAVDP_win.exe --ned ./exp/ned/FeCo/FeCo.lmp -e Fe Co -dw 0.5500 0.5500 -2t 0 150 -l 1.5400 -o ./exp/ned/FeCo/FeCo.ned

>>./bin/AAVDP_win.exe --ned ./exp/ned/FeCo/FeCo_random.lmp -e Fe Co -dw 0.5500 0.5500 -2t 0 150 -l 1.5400 -c 10 10 10 -o ./exp/ned/FeCo/FeCo_random.ned

>>./bin/AAVDP_win.exe --ned ./exp/ned/LaCrGe3/LaCrGe3.vasp -dw 0.7646 0.1028 0.2458 -2t 10 80 -l 2.43955 -o ./exp/ned/LaCrGe3/LaCrGe3_line.ned

>>./bin/AAVDP_win.exe --ned ./exp/ned/LaCrGe3/LaCrGe3.vasp -dw 0.7646 0.1028 0.2458 -2t 10 80 -l 2.43955 -o ./exp/ned/LaCrGe3/LaCrGe3.ned --scherrer -d 400 -d2t 0.02

The selected space group for FeCo is $Pm\bar{3}m$, with a lattice constant of 2.8571Å. The Debye-Waller factors for Fe and Co are both 0.5500 $Å^2$ (at 290K). The wavelengths for both X-ray and neutron beams are set to the default value of 1.54184 Å, to compare the XRD and NED results, as shown in **Fig. 5**. Each diffraction line corresponds to a specific crystal plane index. The NED, compared to the XRD, is able to identify more crystal planes of the ordered FeCo alloy and has a higher resolution in distinguishing the planes. To further compare the two diffraction techniques, an ordered FeCo alloy is generated based on the FeCo alloy. Since the atomic numbers of Fe and Co are close (26 and 27, respectively), the XRD struggles to differentiate between the ordered and disordered FeCo alloys. However, the NED can distinguish between the ordered and disordered FeCo alloys, highlighting the advantage of NED in the study of chemical ordering in alloys.

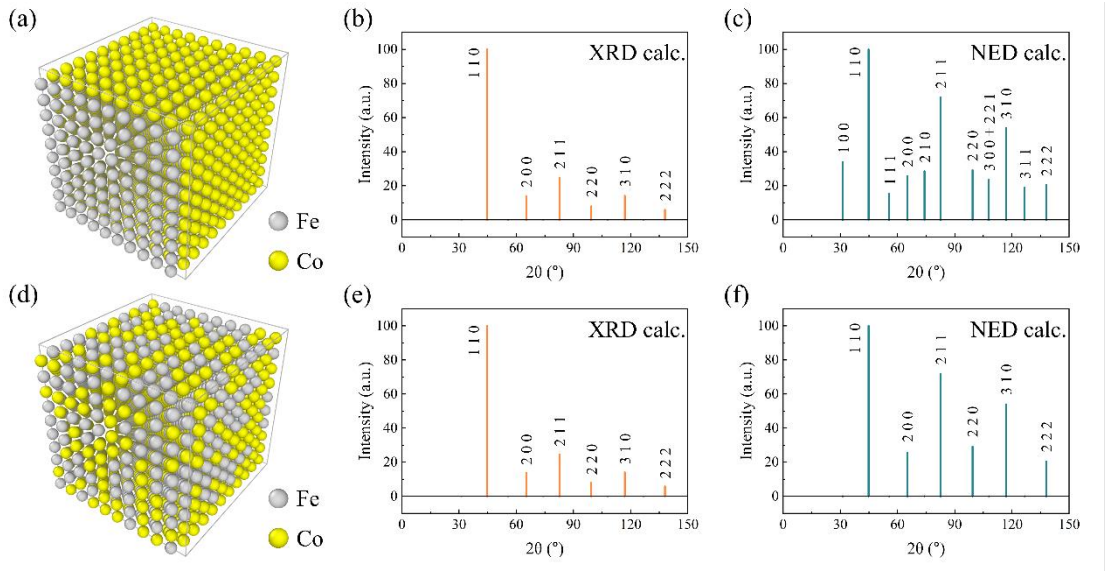

Figure 5. (a) Ordered FeCo alloy; (b) Simulated XRD pattern of ordered FeCo alloy (AAVDP); (c) Simulated NED pattern of ordered FeCo alloy (AAVDP); (d) Disordered FeCo alloy; (e) Simulated XRD pattern of disordered FeCo alloy (AAVDP); (f) Simulated NED pattern of disordered FeCo alloy (AAVDP).

The selected space group for $LaCrGe_3$ is $P6_3/mmc$, with lattice constants of 6.1721Å and 5.7421Å. The test sample is in powder form, and the test conditions are at low temperature (120K), with the neutron beam wavelength set to 2.43955Å. The particle size of $LaCrGe_3$ is unknown, but as shown in **Fig. 6b**, there is broadening of diffraction peaks for various crystal plane indices, indicating the consideration of a certain particle size. As shown in **Fig. 6c**, the results from AAVDP are in good agreement with the experimental data.

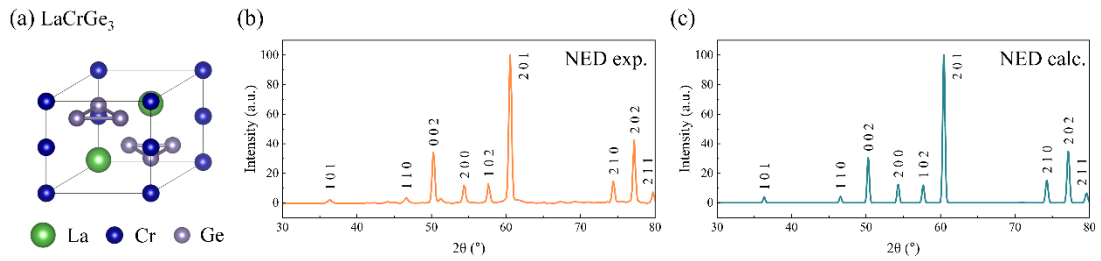

Figure 6. (a) $LaCrGe_3$ crystal structure; (b) Experimental NED pattern of $LaCrGe_3$ [17];

(c) Simulated NED pattern of $LaCrGe_3$ (AAVDP).

5.3 The KED and DED for α-Al_2O_3

This mode demonstrates the KED and DED analyses of the AAVDP program using α-Al_2O_3 crystal material as an example. The commands are as follows:

```
>>./bin/AAVDP_win.exe --ked ./exp/ked/Al2O3/Al2O3.vasp -q 0.8 -o ./exp/ked/Al2O3/Al2O3.001.ked --gauss
>>./bin/AAVDP_win.exe --ked ./exp/ked/Al2O3/Al2O3.vasp -z 2 1 0 -q 0.8 -o ./exp/ked/Al2O3/Al2O3.210.ked --gauss -dx 0.00375 -sig 0.0075 --rotate -x 0 0 1 -y -0.44721360 0.89442719 0
>>./bin/AAVDP_win.exe --ded ./exp/ded/Al2O3/Al2O3.vasp -q 0.8 -o ./exp/ded/Al2O3/Al2O3.001.ded --gauss
>>./bin/AAVDP_win.exe --ded ./exp/ded/Al2O3/Al2O3.vasp -z 2 1 0 -fn 2 1 0 -q 0.8 -o ./exp/ded/Al2O3/Al2O3.210.ded --gauss -dx 0.00375 -sig 0.0075 --rotate -x 0 0 1 -y -0.44721360 0.89442719 0
```

α-Al_2O_3, commonly known as alumina, has a space group of $R\bar{3}c$ with lattice constants of 4.7589Å and 12.9910Å. **Figure 7** compares and contrasts the simulated and experimental diffraction patterns of α-Al_2O_3 for two crystal zone axes, $[0001]$ and $[10\bar{1}0]$. It can be observed that: The simulated and experimental diffraction patterns for the $[0001]$ zone axis are in good agreement. The simulated diffraction pattern for the $[10\bar{1}0]$ zone axis is missing the (003) diffraction spot, which is typically caused by secondary diffraction and has a smaller intensity. When

comparing kinematic and dynamic simulated diffraction patterns, the dynamic simulation's intensity distribution aligns more closely with the experimental results.

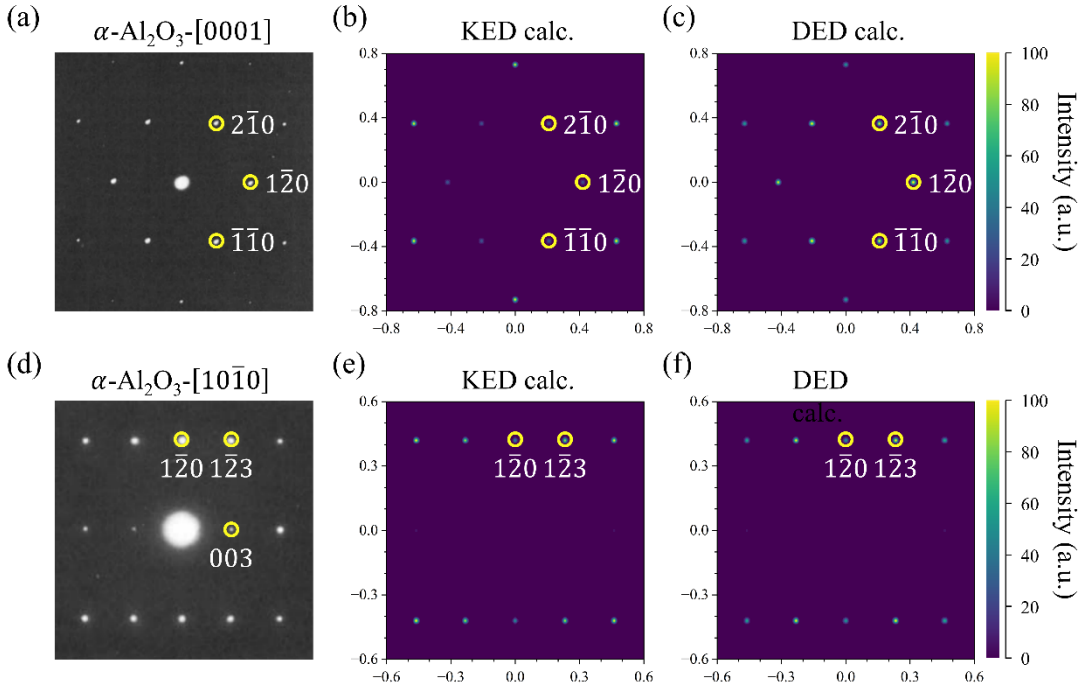

Figure 7. (a) Experimental pattern of α-Al_2O_3 under zone-[0001] [18]; (b) Simulated KED pattern of α-Al_2O_3 under zone-[0001] (AAVDP); (c) Simulated DED pattern of α-Al_2O_3 under zone-[0001] (AAVDP); (d) Experimental pattern of α-Al_2O_3 under zone-[10$\bar{1}$0] [18]; (e) Simulated KED pattern of α-Al_2O_3 under zone-[10$\bar{1}$0] (AAVDP); (f) Simulated DED pattern of α-Al_2O_3 under zone-[10$\bar{1}$0] (AAVDP).

5.4 The KED for Cu{111}<112> and Fe{112}<111> twins

This mode demonstrates the KED analysis of the AAVDP program using Cu{111}<112> and Fe{112}<111> twin models as examples, illustrating the characteristics of twin diffraction spot patterns. The command lines are as follows:

```
>>./bin/AAVDP_win.exe --ked ./exp/ked/Cu_twin/Cu111_twin.lmp -e Cu -z 0 1 0 -
```

```
o ./exp/ked/Cu_twin/Cu111_twin.ked --gauss -sig 0.02 --rotate -x 0 0 1 -y 1 0 0
>>./bin/AAVDP_win.exe --ked ./exp/ked/Fe_twin/Fe112_twin.lmp -e Fe -z 0 1 0 -
o ./exp/ked/Fe_twin/Fe112_twin.ked --gauss -sig 0.02 --rotate -x 0 0 1 -y 1 0 0
```

Twin diffraction spot patterns are actually formed by the overlap of the diffraction spot patterns of the matrix and those of the matrix rotated by 180° around the crystal zone axis. Therefore, twin diffraction spot patterns are symmetric along the inverse vectors corresponding to the twin plane. As shown in **Fig. 8**, the Cu{111}<112> twin diffraction pattern is formed by the overlap of the matrix diffraction pattern with a zone axis of [110] and the diffraction pattern rotated 180° around the zone axis [110], symmetric along the twin plane $(\bar{1}1\bar{1})$. The Fe{112}<111> twin diffraction pattern is formed by the overlap of the matrix diffraction pattern with a zone axis of [011] and the diffraction pattern rotated 180° around the zone axis [011], symmetric along the twin plane $(2\bar{1}1)$, which is in good agreement with the experimental diffraction pattern.

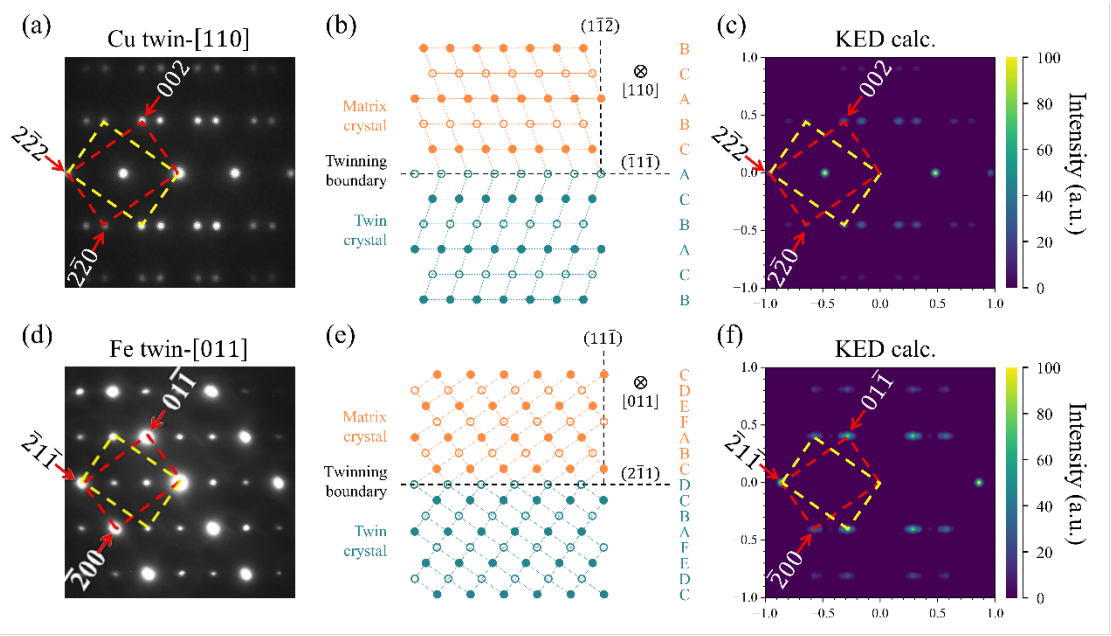

Figure 8. (a) Experimental pattern for Cu{111}<112> twin under zone-[110] [9]; (b) Cu{111}<112> twin structure; (c) Simulated KED pattern for Cu{111}<112> twin under zone-[110] (AAVDP); (d) Experimental pattern for Fe{112}<111> twin under zone-[011] [19]; (e) Fe{112}<111> twin structure; (f) Simulated KED pattern under zone-[011] (AAVDP).

5.5 The KKD and DKD for BCC and HCP crystals

This example demonstrates the KKD and DKD analyses of the AAVDP program using a BCC (Fe). The command lines are as follows:

```
>>./bin/AAVDP_win.exe --kkd ./exp/kkd/bcc/bcc.vasp -q 1.5 -o ./exp/kkd/bcc/bcc.ked3 --ked3
>>./bin/AAVDP_win.exe --kkd ./exp/kkd/bcc/bcc.ked3 -z 1 1 3 -rx 0.25 -ry 0.30 -t 0.3 -px 2000 -py 2400 -o ./exp/kkd/bcc/bcc.113.kkd --rotate -x 0 3 -1 -y 10 -1 -3
>>./bin/AAVDP_win.exe --dkd ./exp/dkd/bcc/bcc.vasp -q 1.5 -z 1 1 3 -rx 0.25 -ry 0.30 -px 500 -py 600 -o ./exp/dkd/bcc/bcc.113.dkd --monte -seed ./RandomSeeds.data -o ./exp/dkd/bcc/bcc.mc --rotate -x 0 3 -1 -y 10 -1 -3
```

Each Kikuchi line in the Kikuchi pattern corresponds to a crystal plane that satisfies the diffraction condition. Therefore, the intersection points of the Kikuchi lines (Kikuchi poles) represent the intersection lines (zone axes) of two crystal planes. The angle between the Kikuchi lines corresponds to the angle between the two crystal planes, and the spacing between the Kikuchi bands is the reciprocal of the interplanar distance. As shown in **Fig. 9**, after calibration, AAVDP provides results that are in

complete agreement with experimental Kikuchi patterns [20]. The KKD pattern primarily reflects the geometric distribution information, while the DKD pattern mainly reflects the intensity distribution information.

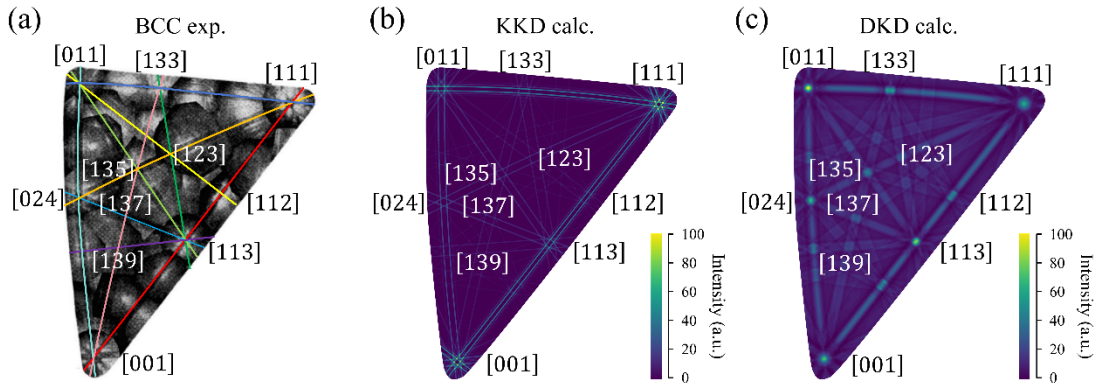

Figure 9. (a) Experimental Kikuchi pattern for BCC [20]; (b) Simulated KKD pattern for BCC (AAVDP); (c) Simulated DKD pattern for BCC (AAVDP).

In addition to the local Kikuchi patterns, AAVDP can also generate global Kikuchi patterns. Here, the BCC structure (Fe) and HCP structure (Zr) are selected as examples to demonstrate the kinematic and dynamic global Kikuchi diffraction analysis capabilities of the AAVDP program. The command lines are as follows:

```
>>./bin/AAVDP_win.exe --kkd ./exp/kkd/bcc/bcc.vasp -q 1.5 -o ./exp/kkd/bcc/bcc.ked3
>>./bin/AAVDP_win.exe --kkd ./exp/kkd/bcc/bcc.ked3 -t 0.3 -px 4000 -py 4000 -o ./exp/kkd/bcc/bcc. kkd
>>./bin/AAVDP_win.exe --dkd ./exp/dkd/bcc/bcc.vasp -q 1.5 -px 600 -py 600 -o ./exp/dkd/bcc/bcc. dkd --monte -seed ./RandomSeeds.data -o ./exp/dkd/bcc/bcc.mc
>>./bin/AAVDP_win.exe --kkd ./exp/kkd/hcp/hcp.vasp -q 1.5 -o ./exp/kkd/hcp/hcp.ked3
```

```
>>./bin/AAVDP_win.exe --kkd ./exp/kkd/hcp/hcp.ked3 -t 0.3 -px 2000 -py 2000 -o ./exp/kkd/hcp/hcp.kkd
>>./bin/AAVDP_win.exe --dkd ./exp/dkd/hcp/hcp.vasp -q 1.5 -px 600 -py 600 -o ./exp/dkd/hcp/hcp.dkd --monte -seed ./RandomSeeds.data -o ./exp/dkd/hcp/hcp.mc
```

As shown in **Fig. 10**, both the kinematic and dynamic global Kikuchi patterns reflect the symmetry information of the BCC and HCP structures.

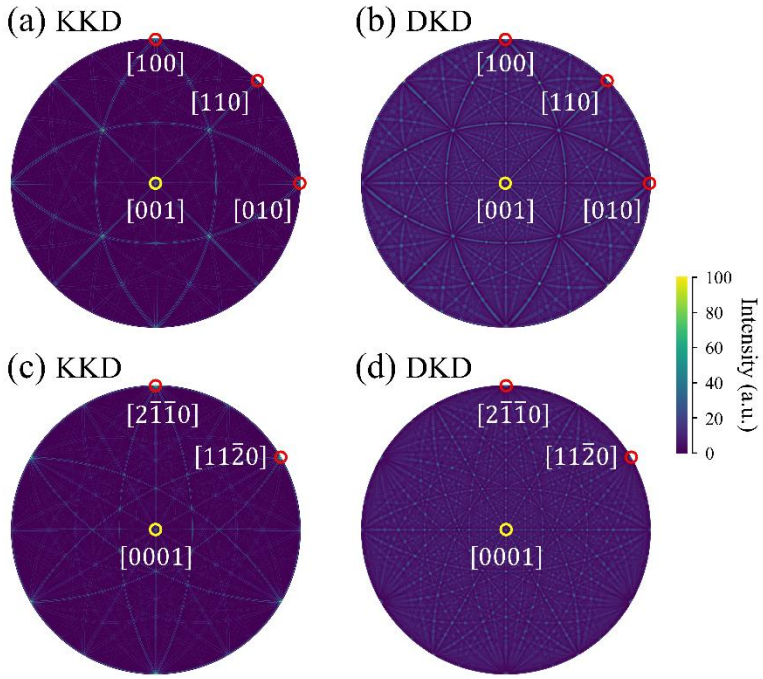

Figure 10. (a) Simulated KKD pattern of BCC (AAVDP); (b) Simulated DKD pattern of BCC (AAVDP); (c) Simulated KKD pattern of HCP (AAVDP); (d) Simulated DKD pattern of HCP (AAVDP).

5.6 The KKD for screw and edge dislocations of FCC structure

To reveal the impact of defect structures on the Kikuchi patterns, the FCC (Fe) crystal model with embedded screw dislocation ($1/6[1\bar{1}2]$) and edge dislocation ($1/2[110]$) is used as an example:

```
>>./bin/AAVDP_win.exe --kkd ./exp/kkd/fcc/fcc.vasp -q 1.5 -o ./exp/kkd/fcc/fcc.ked3
--ked3
>>./bin/AAVDP_win.exe --kkd ./exp/kkd/fcc/fcc.ked3 -z 1 0 0 -rx 0.075 -ry 0.075 -t
0.1 -px 1000 -py 1000 -o ./exp/kkd/fcc/fcc.100.kkd --rotate -x 0.00000000
0.47609129 -0.33664738 -y 0.00000000 0.33664738 0.47609129 --scale -i 0 350
>>./bin/AAVDP_win.exe --kkd ./exp/kkd/fcc/fcc.ked3 -z 0 1 0 -rx 0.075 -ry 0.075 -t
0.1 -px 1000 -py 1000 -o ./exp/kkd/fcc/fcc.010.kkd --rotate -x 0 0 1 -y 1 0 0 --scale -i
0 130
>>./bin/AAVDP_win.exe --kkd ./exp/kkd/fcc/fcc.ked3 -rx 0.075 -ry 0.075 -t 0.1 -px
1000 -py 1000 -o ./exp/kkd/fcc/fcc.001.kkd --scale -i 0 350


>>./bin/AAVDP_win.exe --kkd ./exp/kkd/fcc_screw/screw.vasp -q 1.5 -
o ./exp/kkd/fcc_screw/screw.ked3 --ked3
>>./bin/AAVDP_win.exe --kkd ./exp/kkd/fcc_screw/screw.ked3 -z 1 0 0 -rx 0.075 -ry
0.075 -t 0.1 -px 1000 -py 1000 -o ./exp/kkd/fcc_screw/screw.100.kkd --rotate -x
0.00000000 0.47609129 -0.33664738 -y 0.00000000 0.33664738 0.47609129 --scale
-i 0 350
>>./bin/AAVDP_win.exe --kkd ./exp/kkd/fcc_screw/screw.ked3 -z 0 1 0 -rx 0.075 -ry
0.075 -t 0.1 -px 1000 -py 1000 -o ./exp/kkd/fcc_screw/screw.010.kkd --rotate -x 0 0 1
-y 1 0 0 --scale -i 0 130
>>./bin/AAVDP_win.exe --kkd ./exp/kkd/fcc_screw/screw.ked3 -rx 0.075 -ry 0.075 -t
0.1 -px 1000 -py 1000 -o ./exp/kkd/fcc_screw/screw.001.kkd --scale -i 0 350
```

```
>>./bin/AAVDP_win.exe --kkd ./exp/kkd/fcc_edge/edge.vasp -q 1.5 -o ./exp/kkd/fcc_edge/edge.ked3 --ked3
>>./bin/AAVDP_win.exe --kkd ./exp/kkd/fcc_edge/edge.ked3 -z 1 0 0 -rx 0.075 -ry 0.075 -t 0.1 -px 1000 -py 1000 -o ./exp/kkd/fcc_edge/edge.100.kkd --rotate -x 0.00000000 0.47609129 -0.33664738 -y 0.00000000 0.33664738 0.47609129 --scale -i 0 350
>>./bin/AAVDP_win.exe --kkd ./exp/kkd/fcc_edge/edge.ked3 -z 0 1 0 -rx 0.075 -ry 0.075 -t 0.1 -px 1000 -py 1000 -o ./exp/kkd/fcc_edge/edge.010.kkd --rotate -x 0 0 1 -y 1 0 0 --scale -i 0 130
>>./bin/AAVDP_win.exe --kkd ./exp/kkd/fcc_edge/edge.ked3 -rx 0.075 -ry 0.075 -t 0.1 -px 1000 -py 1000 -o ./exp/kkd/fcc_edge/edge.001.kkd --scale -i 0 350
```

As shown in **Fig. 11**, compared with the Kikuchi patterns of the FCC model, the screw dislocation model shows changes in the Kikuchi patterns along the crystal belt axes $[110]$ and $[\bar{1}11]$ perpendicular to the screw dislocation $1/6[1\bar{1}2]$. Except for the Kikuchi bands corresponding to the $(\bar{1}11)$ and (220) crystal planes, where the intensity remains unchanged, the other Kikuchi bands show a decrease in intensity. In the edge dislocation model, changes are observed in the Kikuchi patterns along the crystal belt axes $[\bar{1}11]$ and $[1\bar{1}2]$ perpendicular to the edge dislocation $1/2[110]$, with intensity reduction in all major Kikuchi bands. The Kikuchi band for the (220) crystal plane exhibits a slight reduction in spacing due to the missing (110) atomic plane caused by the edge dislocation insertion. Additionally, new Kikuchi bands

appear in a small angular range with the Kikuchi pole as the center for crystal planes that are neither perpendicular nor parallel to the (110) plane, resulting in a gradual blurring of the boundary of the region far from the Kikuchi pole. The changes in the Kikuchi patterns reflect the atomic-level effects caused by screw and edge dislocations in the perfect crystal.

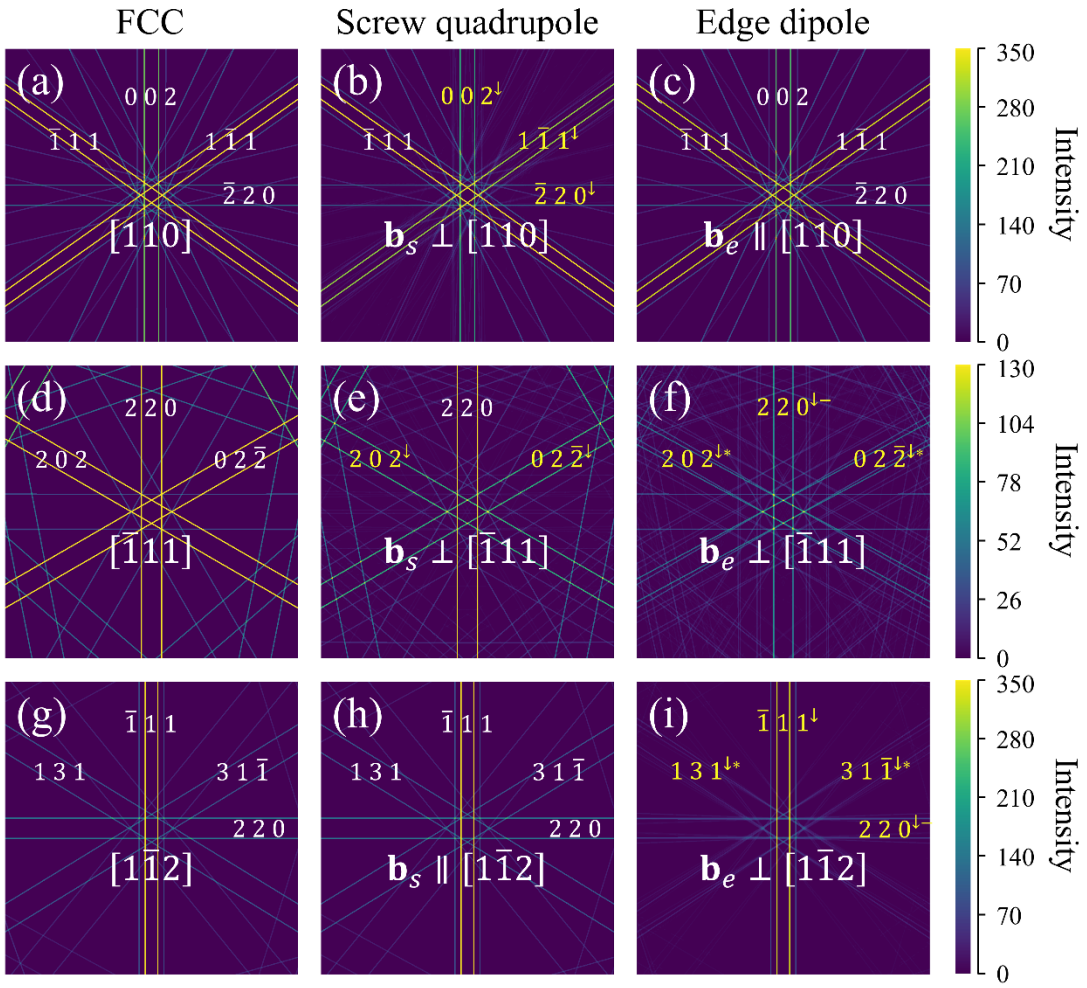

Figure 11. (a) Simulated KKD pattern for FCC model, under zone-[110] (x-axis) (AAVDP); (b) Simulated KKD pattern for screw model, under zone-[110] (x-axis) (AAVDP); (c) Simulated KKD pattern for edge model, under zone-[110] (x-axis) (AAVDP); (d) Simulated KKD pattern for FCC model, under zone-[$\bar{1}$11] (y-axis) (AAVDP); (e) Simulated KKD pattern for screw model, under zone-[$\bar{1}$11] (y-axis)

(AAVDP); (f) Simulated KKD pattern for edge model, under zone-$[\bar{1}11]$ (y-axis) (AAVDP); (g) Simulated KKD pattern for FCC model, under zone-$[1\bar{1}2]$ (z-axis) (AAVDP); (h) Simulated KKD pattern for screw model, under zone-$[1\bar{1}2]$ (z-axis) (AAVDP); (i) Simulated KKD pattern for edge model, under zone-$[1\bar{1}2]$ (z-axis) (AAVDP). ↓ indicates a decrease in Kikuchi band intensity, − indicates a decrease in Kikuchi band spacing, ∗ indicates the boundary of the region far from the Kikuchi pole gradually blurs.

5.7 The RDF for liquid and amorphous crystals in Cu and Cu50Zr50 systems

Here, we select Cu amorphous and liquid states as well as Cu50Zr50 liquid as examples to demonstrate the RDF analysis of the AAVDP program. The command lines are as follows:

```
>>./bin/AAVDP_win.exe --rdf ./exp/rdf/Cu_glass/Cu_glass.lammps -r 8 -n 160 -o ./exp/rdf/Cu_glass/Cu_glass.rdf
>>./bin/AAVDP_win.exe --rdf ./exp/rdf/Cu_liquid/Cu_liquid.lammps -r 8 -n 160 -o ./exp/rdf/Cu_liquid/Cu_liquid.rdf
>>./bin/AAVDP_win.exe --rdf ./exp/rdf/CuZr/Cu50Zr50.liquid.lammps -r 10 -n 100 -partial -o ./exp/rdf/CuZr/Cu50Zr50.liquid.rdf
```

Figure 12 presents the comparison of the RDF for Cu amorphous and liquid states. It can be seen that AAVDP can capture the characteristics of both amorphous and liquid states. The position of the first peak for Cu amorphous and liquid states is

almost identical; however, the former exhibits a higher and narrower peak compared to the latter. The second peak of Cu amorphous state is a splitting peak, while the second peak of Cu liquid state is a mound-shaped peak.

Figure 13 shows the Cu-Zr pair distribution functions calculated by OVITO and AAVDP for Cu50Zr50 liquid, verifying the correctness of AAVDP's calculation results.

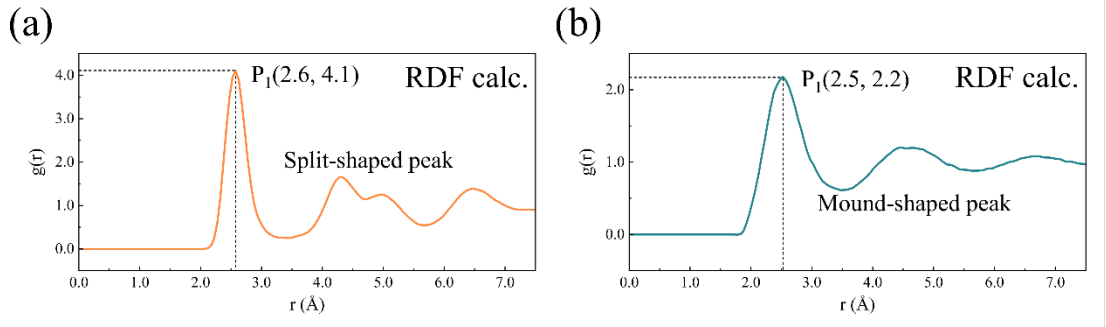

Figure 12. (a) Simulated RDF of Cu amorphous state (AAVDP); (b) Simulated RDF of Cu liquid state (AAVDP).

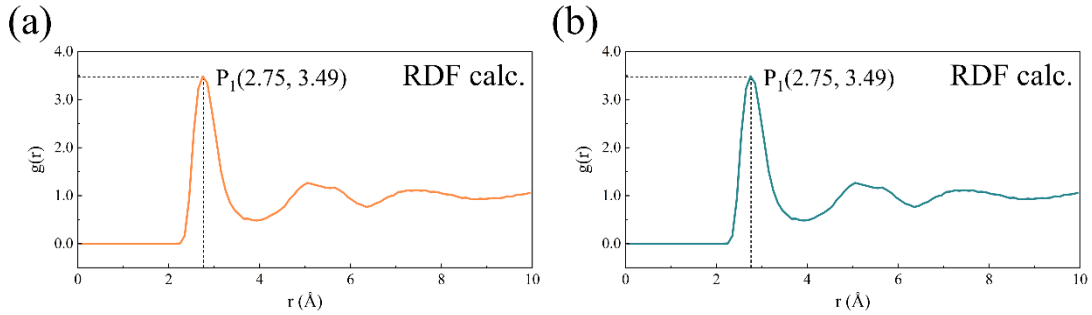

Figure 13. (a) Simulated Cu-Zr pair distribution function of Cu50Zr50 liquid (OVITO) [21]. (b) Simulated Cu-Zr pair distribution function of Cu50Zr50 liquid (AAVDP).

5.8 The SSF for liquid and amorphous crystals in Cu and Cu50Zr50 systems

The following commands are used to demonstrate the SSF analysis of the AAVDP program:

```
>>./bin/AAVDP_win.exe --ssf ./exp/ssf/Cu_glass/Cu_glass.lammps -q 8 -n 160 -o ./exp/ssf/Cu_glass/Cu_glass.ssf --rdf -r 7.5 -n 150
>>./bin/AAVDP_win.exe --ssf ./exp/ssf/Cu_liquid/Cu_liquid.lammps -q 8 -n 160 -o ./exp/ssf/Cu_liquid/Cu_liquid.ssf --rdf -r 7.5 -n 150
>>./bin/AAVDP_win.exe --ssf ./exp/ssf/CuZr/Cu50Zr50.liquid.lammps -q 10 -n 100 -partial -o ./exp/ssf/CuZr/Cu50Zr50.liquid.ssf
```

Figure 14 shows the comparison of the static structure factors for Cu amorphous and liquid systems. It can be observed that AAVDP captures the features of both amorphous and liquid states. The first peak positions of Cu amorphous and liquid are nearly identical, but the peak of the former is higher and narrower. The second peak of Cu amorphous is a splitting peak, while the second peak of Cu liquid is a mound-shaped peak. Additionally, a pre-peak is present before the first peak, which is more pronounced in the amorphous state.

Figure 15 shows the Cu-Zr pair static structure factor for Cu50Zr50 liquid, calculated by previous studies and AAVDP. The overall trend and key features are in good agreement, verifying the accuracy of the AAVDP calculation.

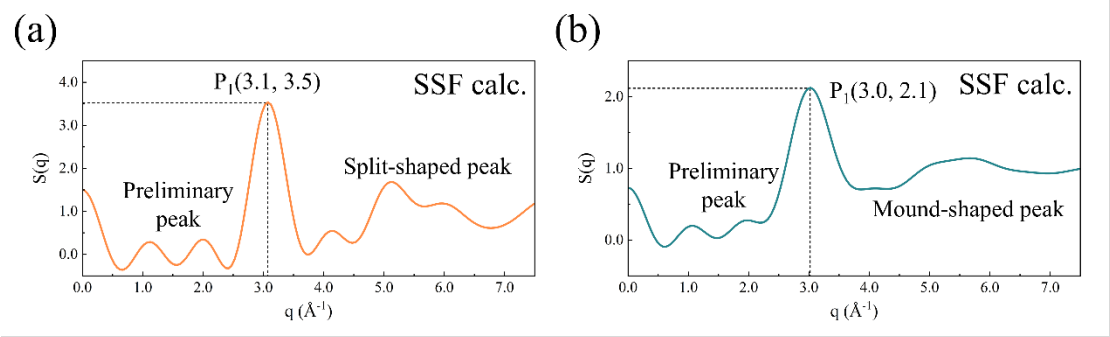

Figure 14. (a) Simulated SSF for amorphous Cu (AAVDP); (b) Simulated SSF for liquid Cu (AAVDP).

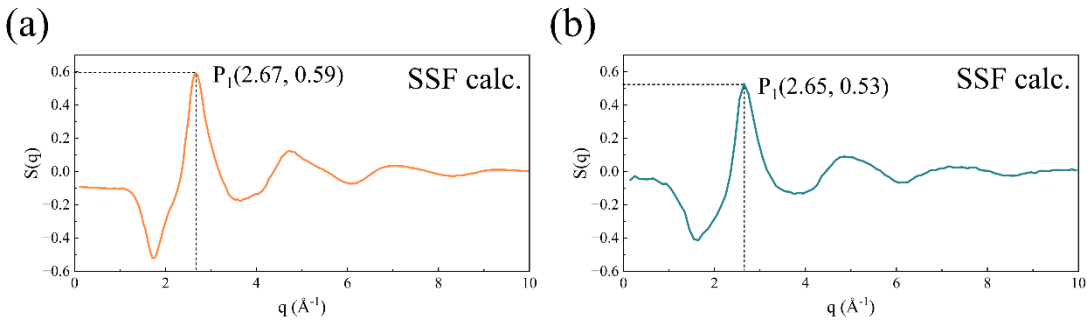

Figure 15. (a) Simulated SSF for Cu-Zr pair in Cu50Zr50 amorphous state [14]; (b) Simulated SSF for Cu-Zr pair in Cu50Zr50 liquid state (AAVDP).

References

[1] Plimpton S. Fast Parallel Algorithms for Short-Range Molecular Dynamics[J]. Journal of Computational Physics, 1995, 117(1): 1–19.

[2] Singh S, Ram F, Graef M D. EMsoft: open source software for electron diffraction/image simulations[J]. Microscopy and Microanalysis, 2017, 23(S1): 212–213.

[3] Liu Z R, Yao B N, Zhang R F. SPaMD studio: An integrated platform for atomistic modeling, simulation, analysis, and visualization[J]. COMPUTATIONAL MATERIALS SCIENCE, Amsterdam: Elsevier, 2022, 210: 111027.

[4] Coleman S P, Spearot D E, Capolungo L. Virtual diffraction analysis of Ni [010] symmetric tilt grain boundaries[J]. MODELLING AND SIMULATION IN MATERIALS SCIENCE AND ENGINEERING, Bristol: IoP Publishing Ltd, 2013, 21(5): 055020.

[5] Doyle P A, Turner P S. Relativistic Hartree–Fock X-ray and electron scattering factors[J]. Acta Crystallographica Section A, 1968, 24(3): 390–397.

[6] Peng L-M, Ren G, Dudarev S L, Whelan M J. Debye–Waller Factors and Absorptive Scattering Factors of Elemental Crystals[J]. Acta Crystallographica Section A, 1996, 52(3): 456–470.

[7] Graef M D, McHenry M E. Structure of Materials: An Introduction to Crystallography, Diffraction and Symmetry[A]. 2004.

[8] Sears V F. Neutron scattering lengths and cross sections[J]. Neutron News, Taylor & Francis, 1992, 3(3): 26–37.

[9] Graef M D. Introduction to Conventional Transmission Electron Microscopy: The transmission electron microscope[A]. 2003.

[10] Weickenmeier A, Kohl H. Computation of absorptive form factors for high-energy electron diffraction[J]. Acta Crystallographica Section A Foundations of Crystallography, INTERNATIONAL UNION OF CRYSTALLOGRAPHY, 1991, 47(5): 590–597.

[11] Spence J C H, Zuo J M. Electron Microdiffraction[M]. 第 1 版. New York: Springer, 1992.

[12] Callahan P G, De Graef M. Dynamical Electron Backscatter Diffraction Patterns. Part I: Pattern Simulations[J]. MICROSCOPY AND MICROANALYSIS, New York: Cambridge Univ Press, 2013, 19(5): 1255–1265.

[13] Abraham F F. An isothermal–isobaric computer simulation of the supercooled-liquid/glass transition region: Is the short-range order in the amorphous solid fcc?[J]. The Journal of Chemical Physics, 1980, 72(1): 359–365.

[14] Zhen-Wei W, Wei-Hua W. Linking local connectivity to atomic-scale relaxation dynamics in metallic glass-forming systems[J]. Acta Phys. Sin., 2020, 69(6): 066101–16.

[15] March N H, Tosi M P. Introduction To Liquid State Physics[A]. 2002.

[16] Akyol M, Ekicibil A, Firat T, Kiymac K. The Structural and Magnetic Properties of $Zn_{0.8-4x}Dy_xO_y$ ($0.05 \leq x \leq 0.10$) Compounds Prepared by Solid-State Reactions[J]. JOURNAL OF SUPERCONDUCTIVITY AND NOVEL MAGNETISM, New York: Springer, 2013, 26(7): 2439–2445.

[17]Cadogan J M, Lemoine P, Slater B R, Mar A, Avdeev M. Neutron diffraction study of the hexagonal perovskite-type compound $LaCrGe_3$[A]. Y. Verbovytskyy, A.P. Goncalves. SOLID COMPOUNDS OF TRANSITION ELEMENTS II[C]. Durnten-Zurich: Trans Tech Publications Ltd, 2013, 194: 71-+.

[18]Lee W E, Lagerlof K P D. Structural and electron diffraction data for sapphire (α-al2o3)[J]. Journal of Electron Microscopy Technique, 1985, 2(3): 247–258.

[19]Zhai K, Zhao K, Zhang Y, Yue J, Zhu P, Li S, Wang C, Cui C, Ping D. Double Diffraction or ω-Fe Diffraction in Body-Centered Cubic {112}⟨111⟩-Type Twinned Martensite[J]. CRYSTAL GROWTH & DESIGN, Washington: Amer Chemical Soc, 2022, 23(1): 539–547.

[20]Okamoto P R, Levine E, Thomas G. Kikuchi Maps for hcp and bcc Crystals[J]. Journal of Applied Physics, 1967, 38(1): 289–296.

[21]Stukowski A. Visualization and analysis of atomistic simulation data with OVITO-the Open Visualization Tool[J]. MODELLING AND SIMULATION IN MATERIALS SCIENCE AND ENGINEERING, 2010, 18(1).